GEORG-AUGUST-UNIVERSITÄT GÖTTINGEN IN PUBLICA COMMODA SEIT 1737

Fakultät für Physik

## Master's Thesis

# Bau & Elektrische Qualitätskontrolle von ITk Pixel Produktionsmodulen

# Assembly & Electrical Quality Control of ITk Pixel Production Modules


prepared by

**Niklas Grün**

from Zeven

at the II. Physikalischen Institut



**Thesis number:** II.Physik-UniGö-MSc-2026/02

**Thesis period:** 1st May 2025 until 30th April 2026

**First referee:** Prof. Dr. Arnulf Quadt

**Second referee:** Prof. Dr. Jörn Grosse-Knetter

# Abstract

Um das ATLAS Experiment auf das Upgrade des LHC am CERN hin zu größerer Strahlintensität (High Luminosity-LHC) vorzubereiten, wird ein komplett aus Silizium Halbleiterdetektoren bestehender InnerTracker (ITk) im Inneren eingebaut werden. Der Pixeldetektor Teil von ITk umfasst neuartige Technologien, so beispielsweise das serielle Powering. Die rund 10.000 Detektormodule werden in einer weltweiten Produktion gebaut und anschließend getestet, insbesondere auf ihre elektrischen Eigenschaften. Im Rahmen dieser Arbeit wurde der SLDO Scan als einer der Tests, die die elektrischen Eigenschaften prüfen, erweitert. Außerdem werden die Stromspiegel im Shuntstromkreis vermessen und die Verstärkungen des Shuntstroms und deren Abhängigkeiten, die in Verbindung mit dem seriellen Powering stehen, untersucht. Als nächstes wird der Modulbau im deutschen Produktionscluster analysiert und die Kompatibilität der im deutschen ITk-Pixel-Produktionscluster eingesetzten Werkzeuge sowie die Produktionsqualität der gebauten Pixel Module systematisch überprüft. Die bisher erzielten Ergebnisse werden zusammengefasst und präsentiert, und redundante Tests sowie Qualitätskontrollkriterien (QC) werden identifiziert. Am Schluss zeigt eine Analyse der Ergebnisse des elektrischen Kaltstarts der Pixel Module, dass diese für den Einsatz im ATLAS Experiment geeignet sind.



**Stichwörter:** ATLAS, ITk, Pixel Detektoren, Modulbau, Elektrische Qualitätskontrolle, Deutsches Produktionscluster



# Abstract

To prepare the ATLAS experiment for the upgrade of the LHC at CERN toward higher beam intensity (High Luminosity-LHC), a completely silicon-based Inner Tracker (ITk), consisting of semiconductor detectors, will be installed in the inner region.
The Pixel detector component of the ITk incorporates novel technologies, such as serial powering. Approximately 10,000 detector modules will be produced worldwide and subsequently tested, particularly with respect to their electrical properties.
Within the scope of this thesis, the SLDO scan, one of the tests used to evaluate electrical characteristics, has been extended. In addition, the current mirrors in the shunt current circuit are characterised, and the gains of the shunt current, along with their dependencies related to serial powering, are investigated.
Furthermore, the module assembly within the German production cluster is analysed, and the compatibility of the tools used in the German ITk Pixel production cluster, as well as the production quality of the assembled Pixel modules, are systematically evaluated. The results obtained so far are summarised and presented, and redundant tests as well as quality control (QC) criteria are identified.
Finally, an analysis of the electrical cold-start results of the Pixel modules demonstrates that they are suitable for operation in the ATLAS experiment.



**Keywords:** ATLAS, ITK, Pixel Detector, Assembly, Electrical Quality Control, German Cluster

# Contents


**1 Introduction** **1**

**2 Theoretical Background** **3**
2.1 The Standard Model . . . . . 3

**3 Experimental Particle Physics with the ATLAS Experiment** **7**
3.1 LHC . . . . . 7
3.1.1 High-Luminosity LHC . . . . . 9
3.2 ATLAS . . . . . 10
3.2.1 Magnet System . . . . . 11
3.2.2 Inner Detector . . . . . 11
3.2.3 Calorimetry . . . . . 13
3.2.4 Muon Spectrometer . . . . . 14
3.2.5 Trigger and Data Acquisition . . . . . 15
3.2.6 Inner Tracker Upgrade . . . . . 15

**4 Semiconductor Pixel Detector** **17**
4.1 Interaction of Particles with Matter . . . . . 17
4.1.1 Massive Particles . . . . . 18
4.1.2 Massless Particles and Radiation . . . . . 19
4.2 Semiconductors . . . . . 20
4.2.1 Doping . . . . . 21
4.2.2 p-n Junction . . . . . 22
4.3 Pixel Detectors . . . . . 23
4.3.1 Signal Generation . . . . . 24
4.3.2 Radiation Damage . . . . . 24

**5 ATLAS ITk Pixel Detector** **27**
5.1 Sensor . . . . . 27
5.2 The ITkPixV2 Readout Chip . . . . . 27

5.3 Bare Module . . . 28
5.4 Flex . . . 29
5.5 Assembly . . . 30
5.6 YARR . . . 31
5.7 Pixel Performance Tests . . . 32
5.8 Local & Production Database . . . 33
5.9 Cell Loading . . . 34

**6 The SLDO Scan and the Mirror Current Factors 35**
6.1 The SLDO Scan . . . 37
6.2 Mirror Current Factor . . . 38

**7 Assembly Analysis 47**
7.1 The FTD in Bonn . . . 47
7.2 Flex Reception . . . 48
7.3 Bare Module Reception . . . 49
7.4 Gluing . . . 50
7.5 Wire Bonding & Pull Testing . . . 52
7.6 Masking & Parylene Coating . . . 54

**8 Electrical Quality Control 59**
8.1 Cold Start-Up Test . . . 59
8.2 Setup . . . 60
8.3 Measurements and Results . . . 61

**9 Conclusion and Outlook 65**

**Appendix**

**A Assembly Guide 73**
A.1 Flex Reception & Metrology . . . 73
A.2 Bare Module Reception & Metrology . . . 75
A.2.1 Vacuum Chuck Alignment . . . 79
A.3 Module Assembly . . . 80
A.3.1 Preparation . . . 80
A.4 Masking . . . 81
A.5 OBWBP . . . 82

# 1. Introduction

Hadron collider experiments such as the ATLAS experiment, further treated in Chapter 3, located at large-scale accelerator facilities, play a leading role in breaking the energy frontiers. Such experiments lead to numerous particle-physics discoveries and are currently the main tool for exploring TeV-scale physics.
The current Run 3 of the Large Hadron Collider (LHC) will deliver an unprecedented wealth of data at a higher energy than previous runs and with improved detector capabilities, which promises a future-oriented success of the LHC physics program. The continuous research at the European Organisation for Nuclear Research (CERN) paves the way for novel explorations of new physics, conducting precise measurements like those of the Higgs boson properties, and performing in-depth analyses of the flavour sector.

To fully exploit its physics potential, the LHC will undergo an upgrade to the High-Luminosity LHC (HL-LHC). According to the current schedule (Fig. 1.1), CERN aims to begin data-taking with the HL-LHC in 2030. The most important advancement of the HL-LHC is the increase in luminosity, which is achieved by more powerful focusing magnets, advanced beam optics and an increased pileup $\mu$. The large amount of data will benefit the statistical uncertainties of ongoing measurements, such as the Higgs boson properties and will also divulge rare events, permitting access to new and exciting physics.

The HL-LHC promises an exciting physics agenda for the next decades, driving scientific progress but demanding the experiments at CERN to operate in extreme circumstances. The increase in luminosity comes along with an intensified amount of radiation, especially in the innermost part of the experiments. This causes more radiation damage in the detector. Moreover, the detector readout capabilities need to be increased significantly to cope with the intensified particle flux and the high hit rates that produce a large amount of data.

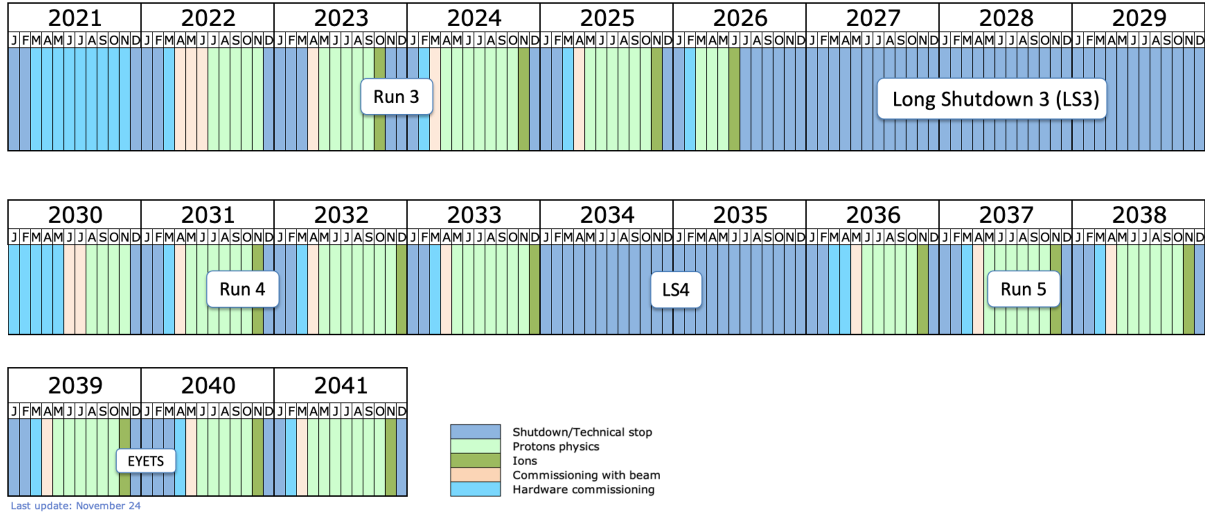


Figure 1.1.: Longterm schedule for the operation of LHC/ HL-LHC ©CERN.

To prepare the ATLAS experiment for the new and enhanced requirements, it is upgraded during the upcoming long shutdown (LS3). A pivotal component for the upgrade is the replacement of the current Inner Detector by an all-silicon Inner Tracker (ITk). The ITk, a project currently in the production phase, consists of silicon Strips and Pixel Detector modules. The Pixel Detector modules feature a hybrid module design, meaning that the sensor is read out via frontend readout chips that are bump-bonded to the sensor.

The actual production and assembly of such modules is spread among numerous physics institutes around the globe and is structured into national clusters. The German cluster, further discussed in Chapter 7, will produce a total of 1,800 Pixel modules for the ITk. To secure high production standards and quality of the ITk Pixel modules, presented in Chapter 5, each of the Pixel modules faces multiple electrical QC check-ups between every major production step on top of non-electrical tests and metrology of the components.

# 2. Theoretical Background

The Standard Model of Particle Physics (SM) encompasses the current theoretical knowledge base of elementary particles. It is the framework for high energy physics and the currently most successful theory to describe the fundamental interactions of particles in the universe.

## 2.1. The Standard Model

The SM is a quantum field theory (QFT) that describes the elementary particles and their interactions based on a Lagrangian [1–13]. It delivers a unified description of three out of the four fundamental forces in the universe: the strong force, the weak force and the electromagnetic force. Only gravity is not (yet) described within the SM. Each of the forces is associated with an underlying symmetry. Following the combined symmetries of the forces, the SM's underlying symmetry is $SU(3)_C \times SU(2)_L \times U(1)_Y$, where $C$ stands for the colour charge, $L$ for left-handedness and $Y$ for the hypercharge. Noether's theorem [14] connects the symmetries with conserved quantities such as the electric charge.

The SM consists of 17 elementary particles. Among those particles, there are 12 particles with half-integer spin, called fermions. The fermion sector of the SM can be divided into two classes: the 6 quarks and the 6 leptons. Together, the 12 fermions make up the matter particles. Both the quarks and the leptons come in 3 generations arranged in weak isospin doublets. Up-type particles have a third weak isospin component $I^3 = +\frac{1}{2}$ and down-type fermions have a weak isospin component of $I^3 = -\frac{1}{2}$ . The up-type quarks (u,c,t) carry an electrical charge of $Q = +\frac{2}{3}$ e, down-type quarks (d,s,b) have a charge of $Q = -\frac{1}{3}$ e [15, 16].
The up-type leptons are the 3 neutrinos $\nu_e$, $\nu_\mu$ and $\nu_\tau$. They are massless according to the SM and electrically neutral. Since they are the up-type leptons, their third weak isospin component is $I^3 = +\frac{1}{2}$. Neutrinos interact exclusively via the weak interaction. The down-type leptons are the charged electron, $\mu$ and $\tau$, which increase in mass with generation; the charge of -1 e is equal for all of them.

On top of that, there are integer spin particles called bosons. Spin-1 vector boson particles are the mediators of the forces. The photon ($\gamma$) is the mediator of the electromagnetic force that is described by quantum electrodynamics (QED). It is massless and has no charge [17–24].
The weak force is mediated by either charged or electrically neutral bosons. The charged $W^+$ and $W^-$ bosons only couple to left-handed particles. The $Z^0$ also couples to right-handed particles and has a different coupling strength to the vector and to the axial-vector component of particles. Both mediators of the weak force, the $W$ as well as the $Z^0$ boson, are massive particles. The weak interaction does not conserve parity, nor CP, unlike the other interactions [3–5].
The weak force and the electromagnetic force can be unified by defining the electroweak hypercharge $Y = 2 \cdot (Q - I^3)$.
Next, the gluon mediates the strong force that is described by the quantum chromodynamics (QCD) [15, 16]. Gluons are massless and do not carry an electrical charge. However, they do carry colour charge, which also enables gluon-gluon self-interactions. In comparison to the electromagnetic force, which has an infinite range, the strong force is short-ranged because gluons themselves carry colour charge, leading to self-interaction and confinement.
Finally, the scalar Higgs boson, the latest addition to the SM [25, 26], has spin-0 and is electrically neutral. The Higgs boson results from the Brout-Englert-Higgs mechanism, that describes how particles acquire their masses [27–32].

The SM describes 3- and 4-point interactions of the elementary particles based on a Lagrangian. The interactions within the framework of the SM are conceptualised and visualised using Feynman diagrams.

For every particle there is an anti-particle, with opposing additive quantum numbers such as the electrical charge, which exists as the negative energy quantum state solution of the Dirac equation. Certain particles are their own antiparticle, like the Higgs boson, since it is a scalar boson and electrically neutral.
Figure 2.1 provides an overview of the 17 elementary particles of the SM with their corresponding masses, charges and spins.

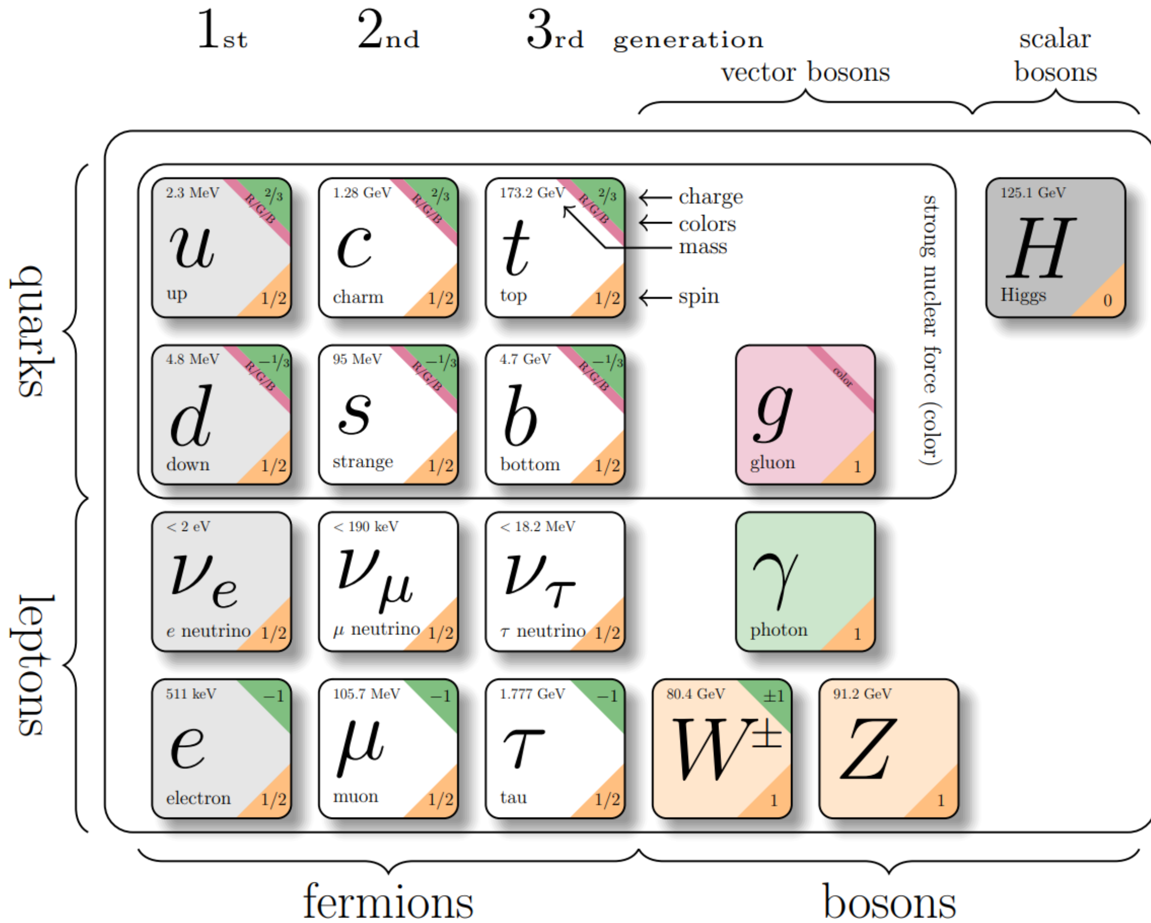


Figure 2.1.: Overview of the SM content [33]. The data are from Particle Data Group [34].

The SM is one the most successful theories in the history of physics and has been probed to extreme limits. So far, the theoretical predictions match the experimental results. Nevertheless, the Standard Model has certain limitations, such as its inability to explain dark matter, neutrino masses, or a quantum theory of gravity. These open questions drive the global search for new physics, for example with the ATLAS experiment at CERN in Geneva.

# 3. Experimental Particle Physics with the ATLAS Experiment

## 3.1. LHC

CERN, the European Organisation for Nuclear Research, is home to the Large Hadron Collider (LHC), the largest and most powerful particle accelerator in the world. Located more than 100 m underground, the LHC can accelerate protons or heavy ions up to nearly the speed of light, giving rise to a centre of mass energy of up to 13.6 TeV. The tunnel of the LHC has a circumference of approximately 27 km. The synchrotron particle accelerator consists of a dual ring with two counter-rotating beams of protons or ions. The beams are not continuous, but they are partitioned into bunches of protons, with a nominal bunch population of $1.2 \cdot 10^{11}$ protons in each bunch [35]. Along the roughly 27 km of the LHC, there are multiple points where the counter-rotating proton beams are brought to collision. Around each collision point, there is a major particle physics experiment. There are 4 main experiments at the LHC: ALICE, ATLAS, CMS and LHCb. The collision frequency is 40 MHz, meaning that the time between two bunch crossings is 25 ns.

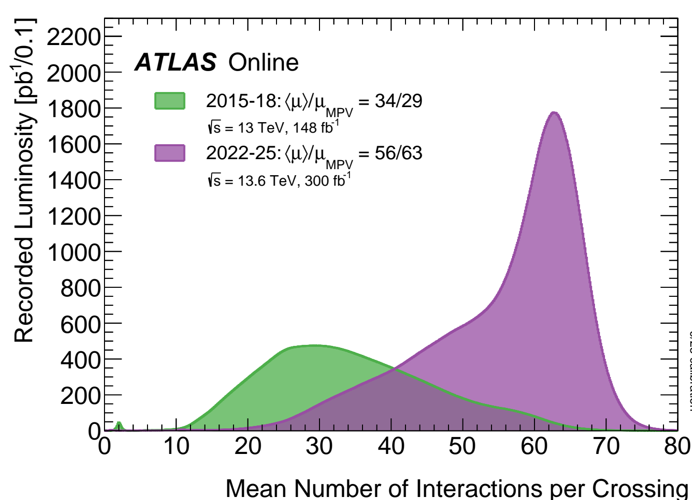


Figure 3.1.: Number of interactions per bunch crossing [36].

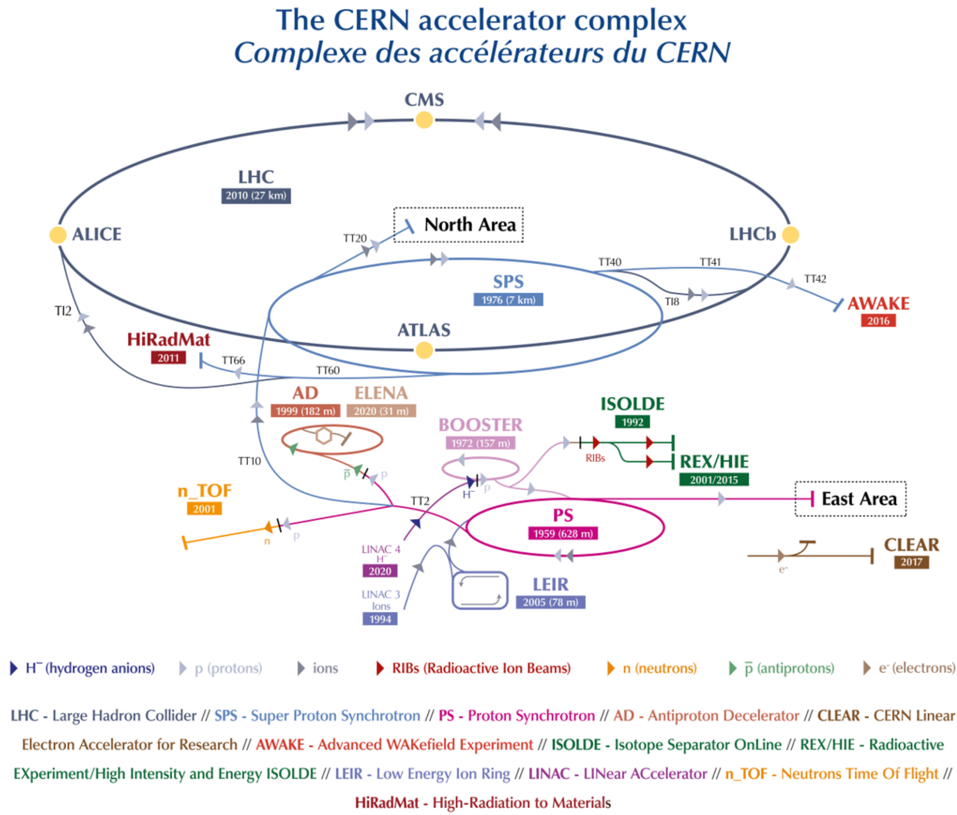


Figure 3.2.: Acceleration chain at CERN ©CERN.

The mean number of interactions per bunch crossing is given by the expectation value of the Poisson distribution describing the number of interactions per crossing, evaluated for each bunch. The distributions for the different data-taking periods are shown in Figure 3.1. To achieve the record-breaking collision energy of 13.6 TeV, the particles run through a complex chain of different pre-accelerators, before they get injected into the LHC ring as illustrated in Figure 3.2. The acceleration of the particles inside the LHC ring happens in high-frequency cavities that have a longitudinal component of the electric field in the direction of motion. The electric wave in the cavities also corrects for potential deviations of the orbital energy and causes a uniform proton energy. Strong, cryogenic magnets keep the particles on their orbit and correct for deviations from the optimal circular movement.

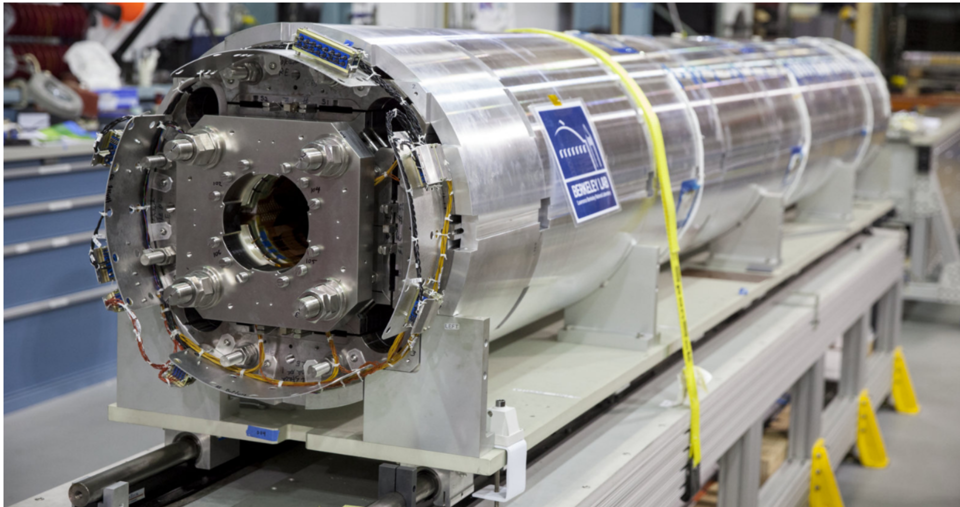


Figure 3.3.: One of the new magnets built by Berkeley Lab, Fermilab, and Brookhaven for the HL-LHC ©Marilyn Sargent/Berkeley Lab.

### 3.1.1. High-Luminosity LHC

The High-Luminosity LHC (HL-LHC) project will start with Run 4 in 2030. It will secure CERN's predominant role in high energy physics, leading both, the energy frontier as well as the hadron collider luminosity peak with an instantaneous luminosity of up to $7.5 \cdot 10^{34}\,\mathrm{cm}^{-2}\mathrm{s}^{-1}$. The HL-LHC, which will serve as a Higgs factory, will give rise to the full physics potential the LHC has to offer. The main motivation and namesake of the HL-LHC is the increased instantaneous luminosity by a factor of 5-7, which results in a targeted integrated luminosity of $4000\,\mathrm{fb}^{-1}$ over 10 years of operation. This increase in luminosity means an unprecedented wealth of data, which will benefit the statistics and will unveil further insights into rare events and phenomena such as $H \to \mu^+\mu^-$. The centre of mass energy will also be increased to 14 TeV.
There are numerous hardware and technology upgrades that together realise the increase in luminosity. Firstly, new and stronger focusing magnets will be installed near the interaction points of ATLAS and CMS, made from $Nb_3Sn$. Figure 3.3 shows one example of such improved magnets. The new magnets provide a stronger field gradient of up to $140\,\frac{\mathrm{T}}{\mathrm{m}}$. The novel sophisticated beam optics near the collision points reduce the beam spot size, fostering head-on collisions. Moreover, a Helium cryogenic plant is installed to provide the cooling power needed for the superconducting magnet systems. On top of that, also the beam instrumentation, monitoring, for example, the new crab cavities and the advanced focusing magnets, is upgraded to provide precise diagnostics and beam position monitoring [35, 37].

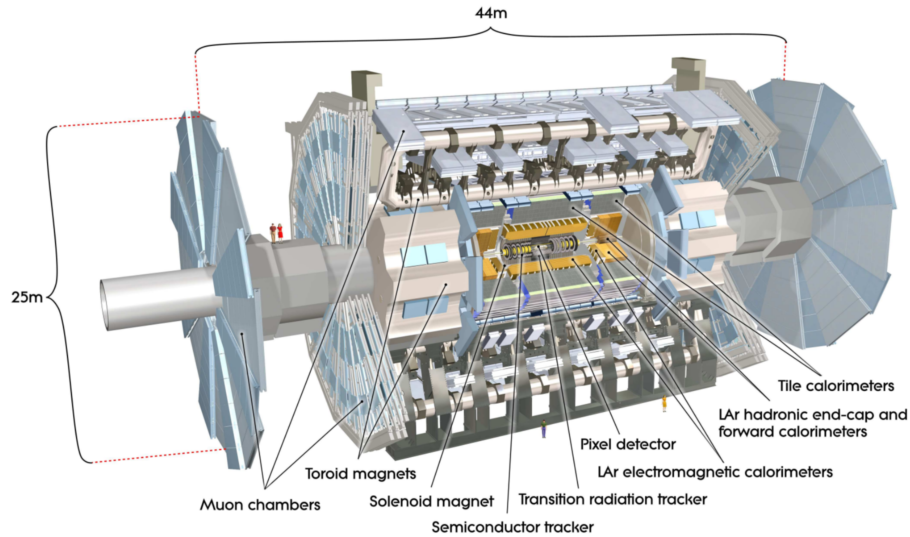


Figure 3.4.: Overview of the ATLAS experiment ©CERN.

## 3.2. ATLAS

The ATLAS experiment, shown in Figure 3.4, is the largest experiment at the LHC. The multi-purpose detector consists of numerous cylindrical layers and endcaps as shown in Figure 3.5, which in emergent combination allow for high precision reconstruction, tracking and energy and momentum resolution.

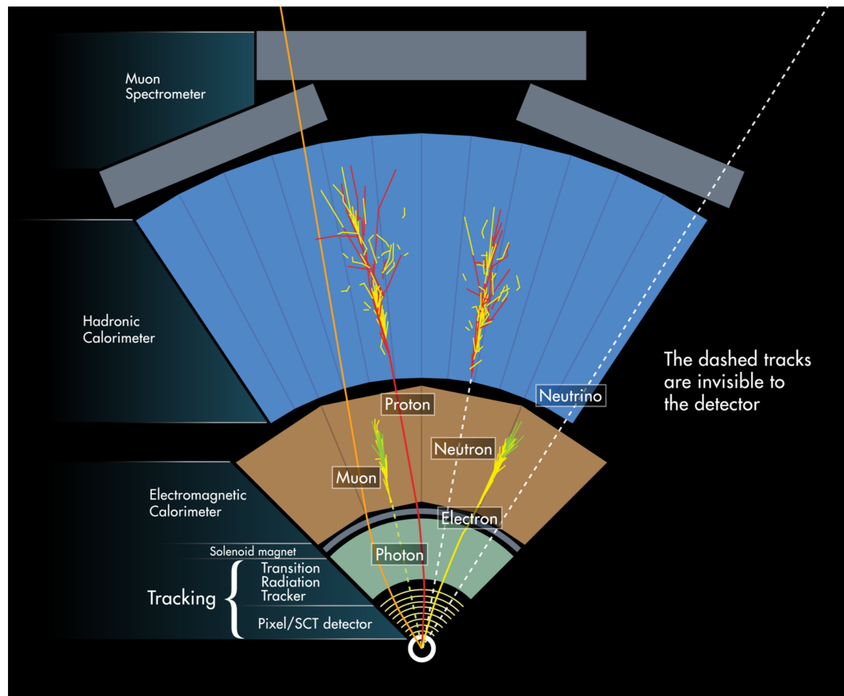


Figure 3.5.: Cross-section of the ATLAS experiment ©CERN.

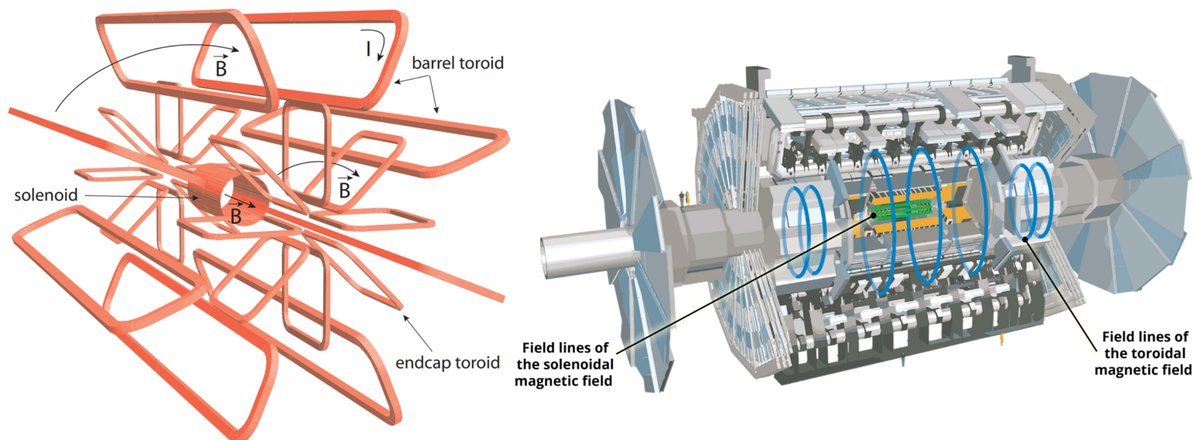


Figure 3.6.: ATLAS magnet system and resulting magnetic field [38, 39].

### 3.2.1. Magnet System

The heart of the ATLAS experiment and the namesake is the magnet system. ATLAS stands for A Toroidal LHC ApparatuS, which indicates that the large magnet system is a toroidal magnet. The toroids cover the barrel and endcaps in a magnetic field of 3.5 T field strength, which is used to deflect muons.
On top of that, the central part of ATLAS features a solenoid magnet system including 4 superconducting solenoids with a magnetic field strength of up to 2 T. The solenoids yield a nearly homogenous magnetic field along the z-axis, so in the beam direction [38, 39]. Figure 3.6 shows the ATLAS magnet system and the magnetic field lines.
In general, magnetic fields are crucial to determine the momentum of charged particles, since they follow a bent trajectory due to the influence of the Lorentz force [40].

### 3.2.2. Inner Detector

The Inner Detector (ID) is the innermost, central part of the ATLAS experiment. The ID environment is characterised by a high track and hit density and intense radiation, demanding the ID to be fast in terms of readout and at the same time particularly radiation hard.
Moreover, the ID has a high spatial resolution, allowing for the exact measurement of vertices and interaction points, which is mandatory for the identification and reconstruction of particles [41]. The ID consists of 3 sub-systems: the Pixel Detector, the SemiConductor Tracker (SCT) and the Transition Radiation Tracker (TRT) as shown in the schematic overview in Figure 3.7.

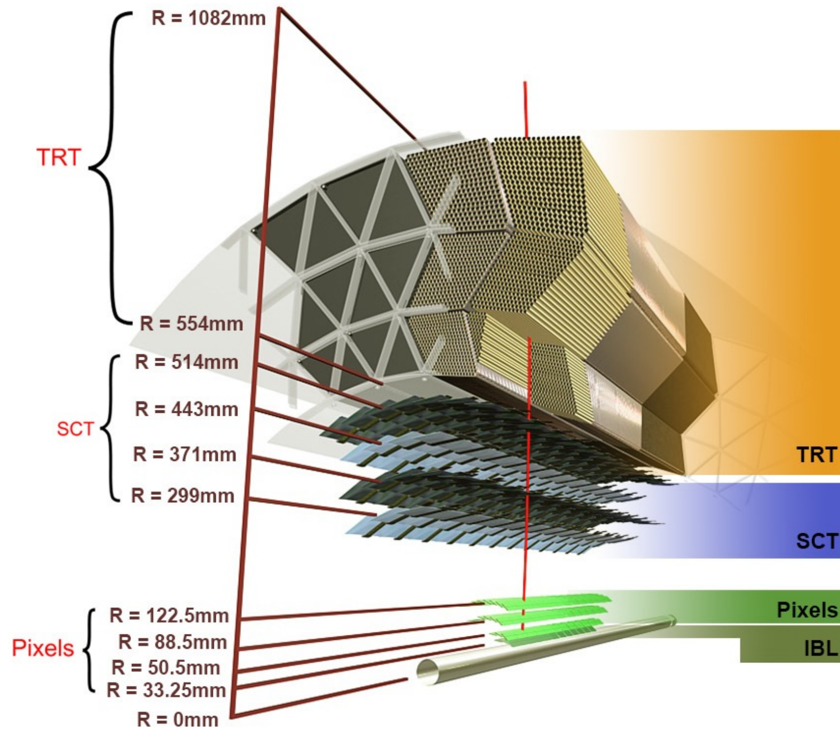


Figure 3.7.: Inner Detector of the ATLAS experiment ©CERN.

### Pixel Detector

The first layers directly encircling the beamline are highly granulated Si Pixel Detectors. The Pixel Detector features three barrel layers and three endcap layers. These three layers comprise more than 1740 modules with a total of roughly 80 million pixels. In addition, the Insertable B-Layer (IBL) was installed during LS1. The IBL has a smaller pixel pitch and delivers an additional 12 million pixels that contribute to advanced precision and tracking resolution. Overall, a spacepoint resolution of 10 µm as well as high momentum precision is achieved with the ATLAS Pixel Detector [42].

### Semiconductor Tracker

The SCT surrounds the Pixel Detector and is made up of Si microstrip detector modules distributed over more than 4000 modules, arranged in four concentric barrel layers and two endcaps with nine disks each [43]. The SCT is dedicated to detecting and reconstructing the track of charge-carrying particles produced in particle collisions. A spatial resolution of $17\,\mu$m is realised with the SCT.
The SCT, in conjunction with the Pixel Detector, makes certain that the particles produced cross a minimum of 4 layers of Si detectors.

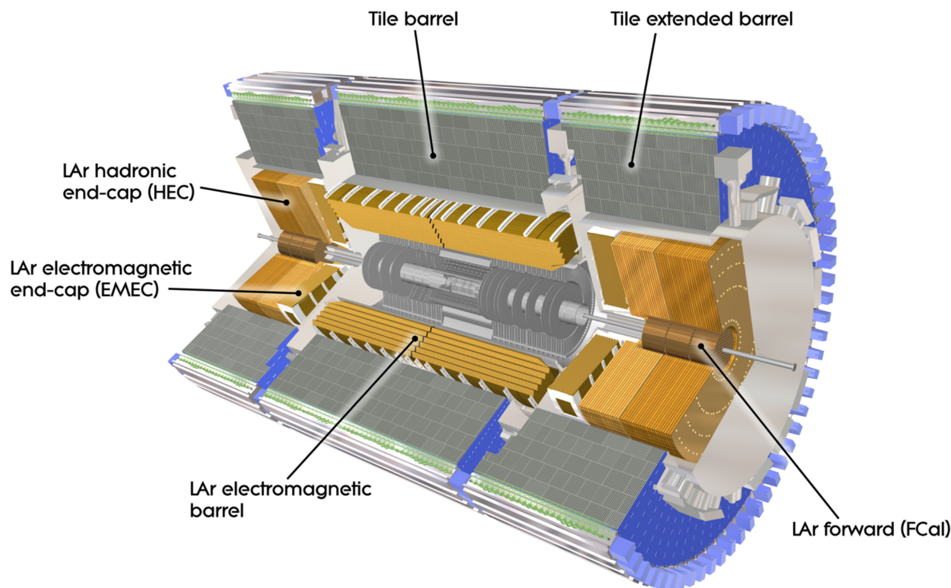


Figure 3.8.: ATLAS calorimeter system ©CERN.

**Transition Radiation Tracker**

Finally, the TRT is the ID's outermost sub-detector, consisting of 300,000 drift tubes ("straws"). The straws are filled with a Xenon-based gas mixture in which electron-ion pairs are created when a charged particle traverses, which creates a detectable electrical signal. The interspace within the straws is filled with polyethylene [44]. When a relativistic particle crosses the interface between the two materials, transition radiation, depending on the Lorentz boost, can be emitted ($\gamma \propto \frac{E}{m}$).
The transition radiation helps to separate, for example, kaons and pions on high energy scales or electrons and charged pions in the regime of 1 to 100 GeV [44, 45].

### 3.2.3. Calorimetry

The calorimeters in the ATLAS experiment determine the energy of neutral and charged particles produced in the collisions and also measure the missing transverse energy, which is crucial for the analysis.
All calorimeters in ATLAS are sampling calorimeters, meaning they consist of alternating layers of active and passive material. The passive material, typically a dense material with a high atomic number, induces cascades of secondary particles (showers), while the active layers measure the deposited energy via ionisation or scintillation light [46].
ATLAS features both an electromagnetic calorimeter (ECal) and a hadronic calorimeter

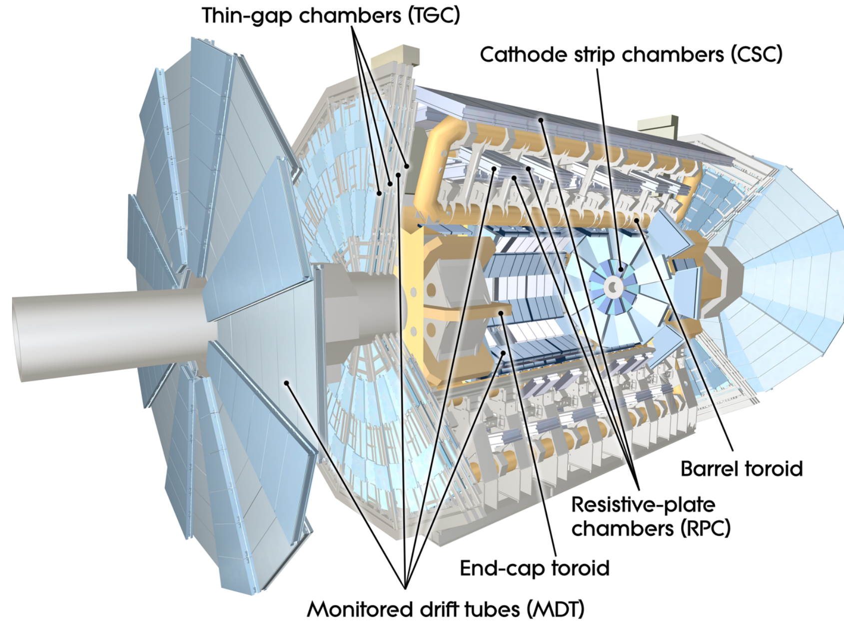


Figure 3.9.: ATLAS muon system ©CERN.

(HCal) to fully capture the particles' energies.
The ECal is designed to measure the energy of electrons, positrons, and photons, using liquid Argon (LAr) as the active medium and Lead as the passive absorber.
The HCal, which measures hadronic showers, has different configurations depending on the detector region. In the barrel region, the HCal employs scintillating plastic tiles as the active medium and steel as the passive absorber. The hadronic endcap and forward calorimeters, on the other hand, use LAr as the active medium, with Copper serving as the passive absorber in the endcap and a combination of Copper and Tungsten in the forward calorimeter [41]. With the exception of muons, which are highly penetrating, all particles produced in the collisions are fully absorbed within the calorimeter system. Figure 3.8 illustrates the ATLAS calorimeter systems.

### 3.2.4. Muon Spectrometer

Lastly, the outermost layer of ATLAS functions as a muon detector. As illustrated in Figure 3.9, muons pass through the previous detector layers because they are minimum ionising particles (MIPs), depositing very little energy and interacting minimally with matter. The gas-filled detectors of the muon spectrometer become ionised as muons pass through, leaving behind a bent track due to the influence of the Lorentz force in the strong magnetic field of the air-core toroids. Tracking with these gaseous detectors allows for precise measurement of the muon's position and momentum [47].

### 3.2.5. Trigger and Data Acquisition

The high collision frequency of 40 MHz paired with the enormous event rate of up to 1.7 billion proton-proton collisions per second outperforms any computational capacity. Since most of the processes that appear are well known and therefore not of particular scientific interest, the data and events are filtered by a multi-layer trigger system. Relevant or interesting events are sorted out either on the software or the hardware level, such that the output data is reduced to a manageable amount, which is then stored for analysis. The Level 1 (L1) trigger, a hardware-based system, selects high-priority events such as high-$p_T$ muon events at a rate of approximately 100 kHz, reducing the data rate. In contrast, the High Level Trigger (HLT), a software-based system, further refines the event selection using more complex algorithms and signatures, allowing for more precise event rejection or acceptance. In total, the trigger system reduces the event rate from 40 MHz to 1000 Hz. The subset of events that are not filtered out by the trigger system is stored at the CERN data centre for further investigation [48].

### 3.2.6. Inner Tracker Upgrade

As presented in the timeline in Figure 1.1, the LHC is facing a long shutdown (LS) from 2026 on. During the shutdown period, several substantial upgrades are performed, which are not just limited to the LHC but also prepare the ATLAS experiment for the new chapter of advanced particle physics research.
The HL-LHC, with its stronger beam focusing, resulting in more collisions, which will catapult the amount of data that is collected, forces the LHC detector experiments, such as ATLAS, to meet new demands on the radiation tolerance and the treatable data rate because of the intensified amount of radiation.
To be fully prepared for the high luminosity phase of the LHC, the ATLAS experiment is also upgraded in parallel with the LHC in the same shutdown period before restarting data taking in 2030. A pivotal component of this upgrade is the replacement of the ATLAS ID with an inner tracker consisting entirely of Silicon semiconductor detector modules called ITk. Currently, the ITk project faces an intense production phase.

The ITk layout features 5 barrel layers of hybrid silicon Pixel Sensors, which are the main subject of this work and are further treated in Chapter 5, with additional pixel endcaps surrounded by 4 layers of silicon Strip detectors, as shown in the layout (Figure 3.10), plus 6 endcap disks per side.

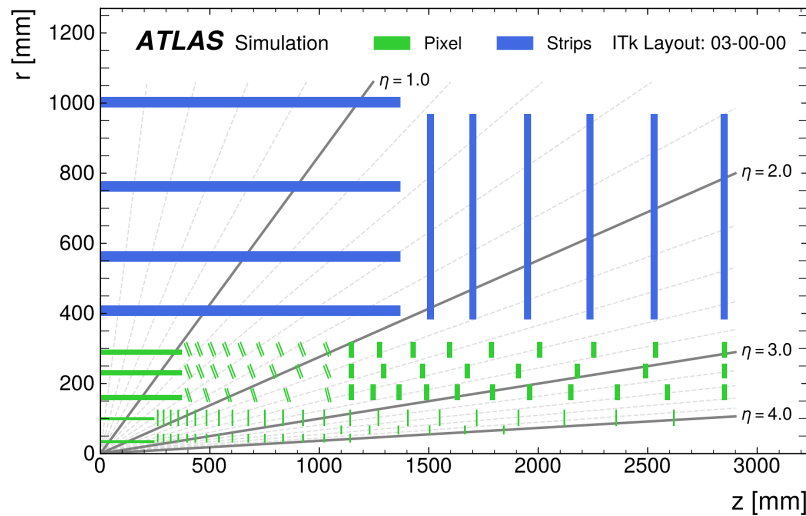


Figure 3.10.: Layout of the ITk ©CERN.

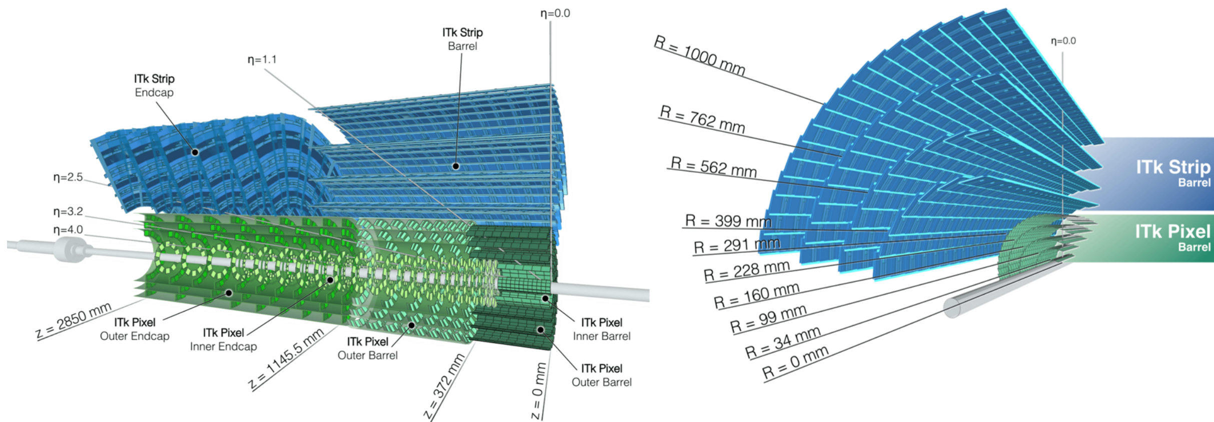


Figure 3.11.: Illustration of the ITk. It will consist of approx. 10,000 modules, which are Strips and Pixels ©CERN.

The Pixel and Strip detector modules are installed on low mass carbon-fibre support structures that feature the $CO_2$-based bi-phase cooling system to secure a reliable operation temperature of $-15\,°C$ to limit leakage current and noise. Moreover, to cope with the large data rate, the electrical detector signals are converted into optical signals to enable high-speed optical links with up to 10.24 Gbps readout.
Essentially, the ITk upgrade enhances every aspect of ATLAS tracking performance, achieving a track reconstruction efficiency of 98% even under conditions with 200 pile-up interactions. The improved vertexing will benefit the b-tagging and the $\tau-$identification, both crucial aspects, especially in the top and Higgs analyses. Figure 3.11 provides an overview of the ITk layout.

# 4. Semiconductor Pixel Detector

Detectors count, track and identify particles that are produced, for example, in collider experiments.
This chapter is dedicated to an introduction to semiconductor Pixel Detectors, one of the many detector forms used in modern particle physics experiments. The necessary conceptual and theoretical background is introduced to understand the ATLAS ITk Pixel modules in more detail, which are examined within the scope of this thesis.

## 4.1. Interaction of Particles with Matter

The particle detection stems from the particles' interaction with the detector material. The specific interaction that determines the measuring process depends on the particle type, its energy and the detector material.
There are three main interactions between radiation and matter.

**1. Ionisation and Excitation** happen when an incoming particle transfers (part of) its energy to an electron, most likely of an outer shell electron, of the detector material's atoms, such that it gains enough energy to escape the binding atomic potential. The remaining Ion is charged, as a neutral atom loses a charge-carrying particle.

**2. Bremsstrahlung** is electromagnetic radiation emitted when charge-carrying particles are decelerated due to deflection by a charge carrier, in most cases, an electron by an atomic nucleus.

**3. Photoelectric effect** describes the emission of electrons when a material is hit by electromagnetic radiation above a certain energy. This is when the photon has an energy above the binding energy of the electron to the nucleus.

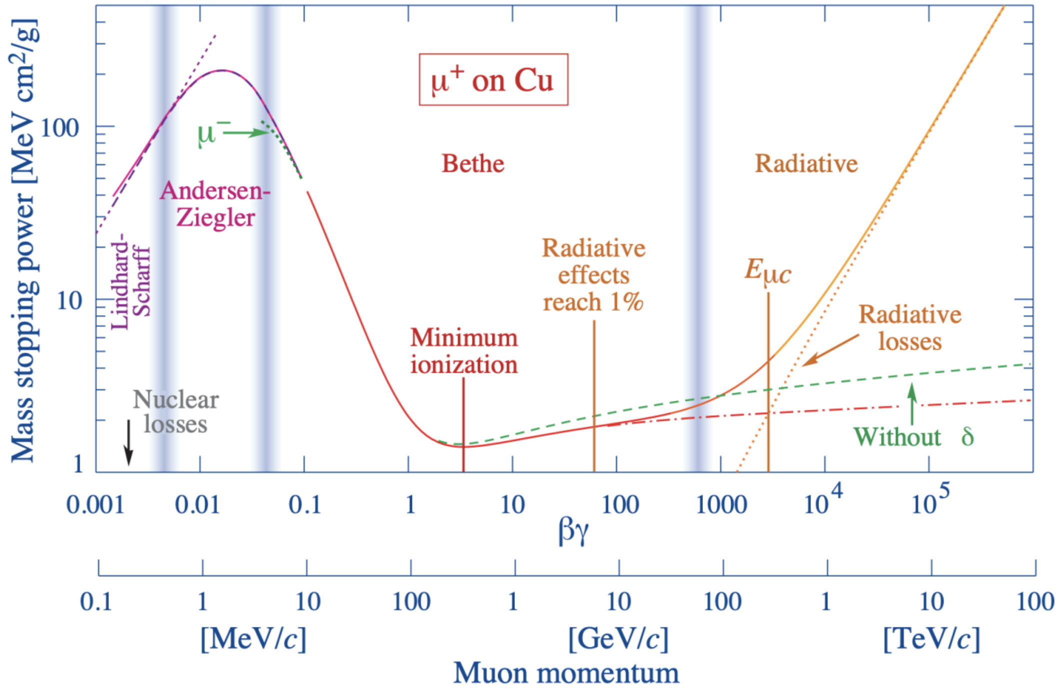


Figure 4.1.: Mean energy deposition of a muon in Copper according to Bethe Bloch [49].

### 4.1.1. Massive Particles

The mean energy deposition of relativistic charged massive particles traversing matter, for example, the detector material, is described by the Bethe-Bloch-Formula [50, 51]:

$$-\left\langle \frac{\mathrm{dE}}{\mathrm{dx}} \right\rangle = \frac{4\pi n z^2}{m_e c^2 \beta^2} \cdot \left( \frac{e^2}{4\pi\varepsilon_0} \right)^2 \cdot \left[ \ln \left( \frac{2 m_e c^2 \beta^2}{I(1-\beta^2)} \right) - \beta^2 - \delta \right], \tag{4.1}$$

where $\beta = \frac{v}{c}$, $n = \frac{N_A \cdot Z \cdot \rho}{M_u \cdot A}$ is the electron density, $I$ is the mean excitation energy, which can be approximated to $I = 10\,\mathrm{eV} \cdot Z$ and $\delta$ describes the density corrections to the mean energy loss due to relativistic polarisation effects, which are particularly relevant at high energies [51].
The mean energy deposition depends on a particle's charge, its type and also its energy. The deposited energy in the detector material causes excitation and ionisation and creates electron-hole pairs in the semiconductor that are subsequently used in the detection process. The average energy to create an electron-hole pair in Si is 3.65 eV and therefore larger than the bandgap of Si with 1.12 eV such that the electrons are lifted from the valence to the conduction band. The distribution of the mean energy deposition of a particle has a minimum at $\beta\gamma \approx 3.5$. Such particles are called minimum ionising particles (MIPs) [46].

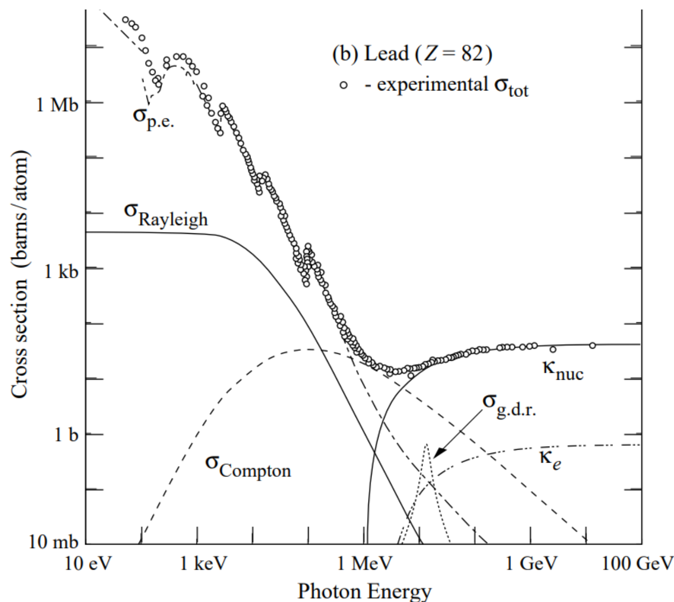


Figure 4.2.: Cross section for possible interaction of photons plotted against the photon energy [46].

Since a MIP's mean energy deposition is the least, they are especially hard to detect. Typically, most hadrons and muons produced in LHC collision experiments are either MIPs or behave MIP-like when their $\beta\gamma$ value is close to that of a true MIP. Consequently, it is especially important to optimise the detectors to accurately register these MIPs.

### 4.1.2. Massless Particles and Radiation

The massless photons, emitted in QED processes, show three main interactions with material: the photoelectric effect, Compton scattering and pair production. Which of these interactions occurs primarily strongly depends on the photon's energy, as shown in 4.2.

**Photoelectric effect:** The photoelectric effect describes that if the initial photon has enough energy $E_\gamma$, which is transferred to an atom's electron, the electron energy is sufficient to escape the binding atomic potential of energy $E_{bind}$. Consequently, the emitted electron has a kinetic energy of $T = E_\gamma - E_{bind}$. The photoelectric effect is dominant in the energy regime of up to approximately 100 keV.

**Compton scattering:** In Compton scattering, an incoming photon interacts with a lightly bound outer-shell electron, transferring part of its energy to the electron and ejecting it from the atom. The photon then propagates on at a different angle with

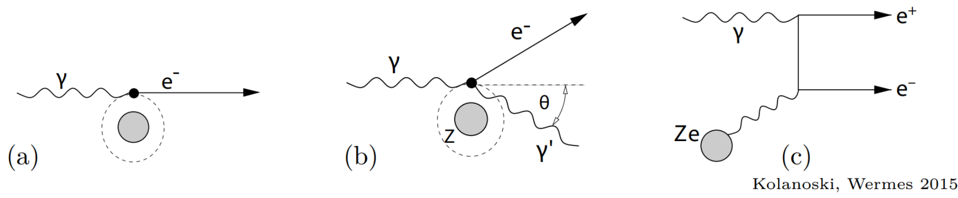


Figure 4.3.: Feynman diagrams for the three photon interactions [46].

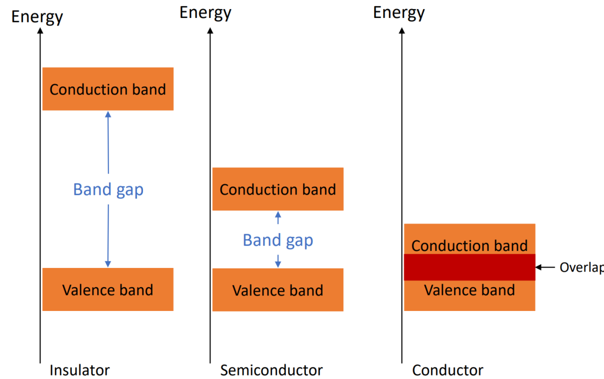


Figure 4.4.: Bandgap comparison for conductor, semiconductor and insulator.

reduced energy, corresponding to an increase in its wavelength. Compton scattering is the dominant process between roughly 100 keV and several MeV.

**Pair production:** In the Coulomb field of a nucleus, a high energetic photon can split up into an electron-positron pair. The energetic threshold for this process corresponds to twice the electron mass of about $m_e = 511\,\text{keV}$, so the photon energy must exceed $E_\gamma > 1.022\,\text{MeV}$. Thus, the pair production becomes dominant at energies in the MeV regime.

The three photon interactions are visualised with corresponding Feynman diagrams in Figure 4.3.

## 4.2. Semiconductors

Semiconductors, whose electrical conductivity lies between that of insulators and that of conductors, have a small band gap between the valence and the conduction band as illustrated in Figure 4.4. The band gap is an energy interval that can not be occupied by electrons. There are different semiconductors, such as Germanium or Gallium Arsenide, but the most important semiconductor and current industry standard is Silicon (Si). The

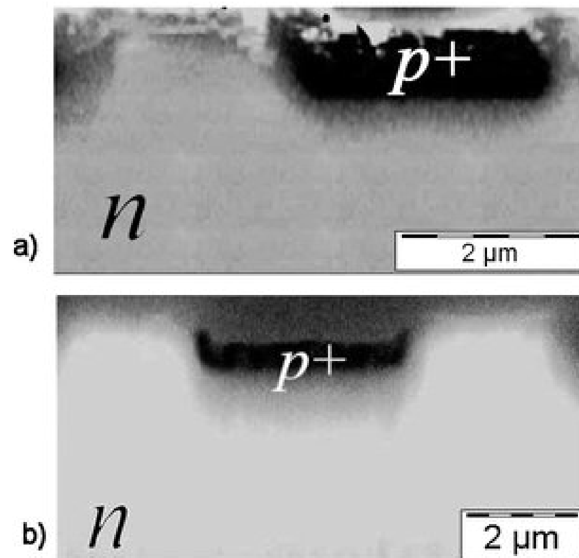


Figure 4.5.: p-well in a n-type doped semiconductor substrate [52].

Si-based semiconductor industry today allows for the growing computational resources in the data and information technology-dominated era.

### 4.2.1. Doping

The electrical properties of semiconductors can be intentionally modified through doping, by introducing atoms into the pure semiconductor crystal lattice that have a different number of valence electrons than the host atoms, most commonly Si. There are two types of doping: n-type and p-type doping. n-type doping means that the inserted atoms have more valence electrons than Si, mostly done with Phosphorus (P). p-type doping, on the other hand, means intentionally inserting atoms with fewer valence electrons than Si, commonly Boron (B) [46].

Moreover, the doping concentration has a strong influence on the semiconductor's behaviour. The doping concentration is indicated with '+' or '-', where '+' indicates a high doping concentration and '-' labels a lowly doped semiconductor. For example, 'n+' marks a strongly n-type doped semiconductor.
Localised sections or areas within a semiconductor substrate that are doped or doped differently than the rest of the substrate are called 'well'. Figure 4.5 shows a p-well in an n-type doped substrate.

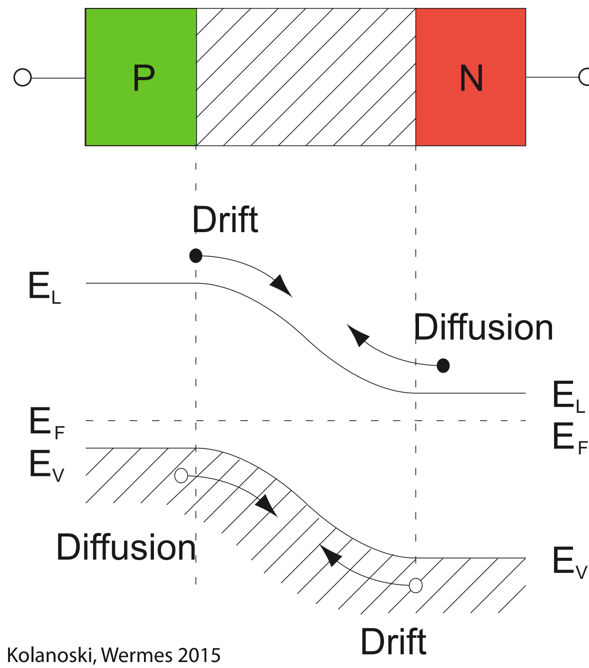


Figure 4.6.: p-n junction with diffusion and drift [46].

### 4.2.2. p-n Junction

The combination of a p-type and n-type doped semiconductor creates a p-n junction. The diffusion of the electrons and holes causes an intrinsic electric field between the doped semiconductors opposing the diffusion direction, causing a drift in the opposite direction, as shown in Figure 4.6. In equilibrium, both processes balance, leaving a depletion zone with a positive and a negative charge at the interface. This depletion region has no free charge carriers left. The depletion zone extends primarily towards the lower-doped semiconductor substrate. Thus, a lowly doped substrate is desired for full depletion. One can further apply an electric field to the doped semiconductors. The depth of the depletion region depends on the doping concentration and the applied voltage and its direction.
Furthermore, the conduction current depends on the voltage and its direction. In reverse bias, the reverse leakage current is comparatively small up to a certain breakdown voltage. The leakage current is approximately constant for a constant temperature, but increases exponentially when the temperature rises [53]. When the reverse bias voltage is increased even further, the resulting electrical field gets so large that the p-n junction is destroyed, which is referred to as the breakdown voltage [54]. Figure 4.7 shows a measured IV curve taken with an ATLAS ITk Pixel Bare Module.

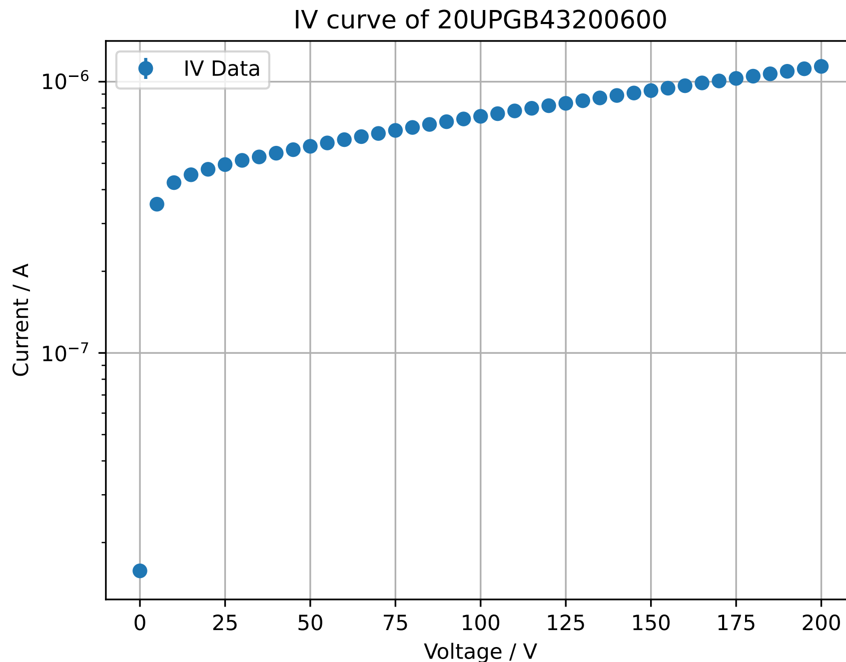


Figure 4.7.: IV-curve between 0 and 200 V bias voltage, taken with a Bare Module (Sensor-Chip-hybrid) at the FTD in Bonn.

## 4.3. Pixel Detectors

Pixel Detectors are one specific type of semiconductor detectors. They allow for high spatial resolution due to fine segmentation of the sensor material. Pixel Detectors are the current standard for the innermost layers of collider experiments. The environment in which Pixel Detectors are installed is characterised by a high flux of particles and heavy radiation. Pixelating the sensor material allows for coping with the intense hit rate and also avoids too large an occupation of the single pixels. Nevertheless, the Pixel Detectors still produce a large amount of data and have a high rate of data transmission, which makes fast readout mandatory. The field of Pixel Detectors can be divided into two branches. On the one hand, there are Monolithic Active Pixel Detectors (MAPS), which are characterised by the sensor and the readout implemented on the same substrate. On the other hand, there are hybrid Pixel Detectors. Hybrid Pixel Detectors have a disjoint sensor and readout, meaning that the chip and the sensor form two different entities. The two parts of the Pixel Detector are interconnected with bump bonds, which are small metal blobs that are melted to permanently connect the sensor and the chip. Hybrid Pixel Detectors are more radiation tolerant, which makes them the preferred choice for collider experiments with high luminosity, such as the ATLAS experiment.

### 4.3.1. Signal Generation

In most cases, the detector material is lightly n-type doped silicon installed between two electrodes that are the source of an applied voltage. The charge-collecting electrodes are used for the readout. In the default case, readout is at the anode. An incoming ionising particle creates electron-hole pairs by lifting electrons from the valence to the conduction band since the energy per electron-hole pair excitation is around 3.65 eV and therefore higher than the band gap in Si (1.12 eV).
The intrinsic or applied electric field separates the electrons and holes. Assuming a constant electric field, the drift motion performed by the charge carriers towards the electrodes has an approximate constant velocity. By segmentation of the doped electrode, it is possible to achieve very high spatial resolution.
The measured signal is a current induced by the moving charge carriers, described by the Shockley-Ramo theorem [55, 56]. The challenge for the signal generation is to separate the real signal originating from the ionisation of a fast charged particle traversing the detector from the background and noise. There are diverse sources of noise. Primarily, thermal fluctuations cause thermal noise. Shot noise is specific to semiconductors and is caused by statistical fluctuations in the number of charge carriers (electrons or holes) passing through a junction or conducting region over time.

### 4.3.2. Radiation Damage

As semiconductor detectors are often installed near the beam pipe, for example, at the Atlas experiment, they are exposed to a high particle flux and intense radiation, which harms the detector material. Part of the radiation damage is reversible, while damage from non-ionising energy loss (NIEL) is not. NIEL happens through collisions with the silicon crystal lattice, which leads to vacancies and interstitials between lattice atoms. The collision processes are Coulomb scattering and elastic as well as inelastic scattering of nuclei. High-energy nucleons and nuclei can kick an atom out of its crystal lattice. If enough energy is transferred, the kicked-off atom can kick further atoms off the lattice, creating a cluster of radiation damage in the semiconductor crystal lattice, as shown in Figure 4.8. Different particles cause a different number of vacancies. Although the average energy transfer for protons is much smaller than that for neutrons, protons are responsible for many more vacancies, because the cross-section for Coulomb scattering is much larger than the cross-section for (in-)elastic neutron scattering. As a consequence, protons and electrons create more point defects than neutrons. To respect the diverse particles causing radiation damage and their different effects, the radiation damage is normalised to

neutron equivalents (neq), which corresponds to the damage caused by 1 MeV neutrons. Therefore, the radiation hardness is determined in units of neq. Due to the missing atoms leaving more holes in the lattice, the doping concentration can change and thus might subsequently lead to type inversion from n-type to a p-type doped semiconductor. Moreover, radiation damage can cause permanent deep-level traps that can catch electrons or holes created from primary ionising particles. The trapped charge carriers subsequently do not contribute to the signal generation, since their drift motion is stopped by the trap, or if they are released from the trap, their contribution to the signal generation is delayed.

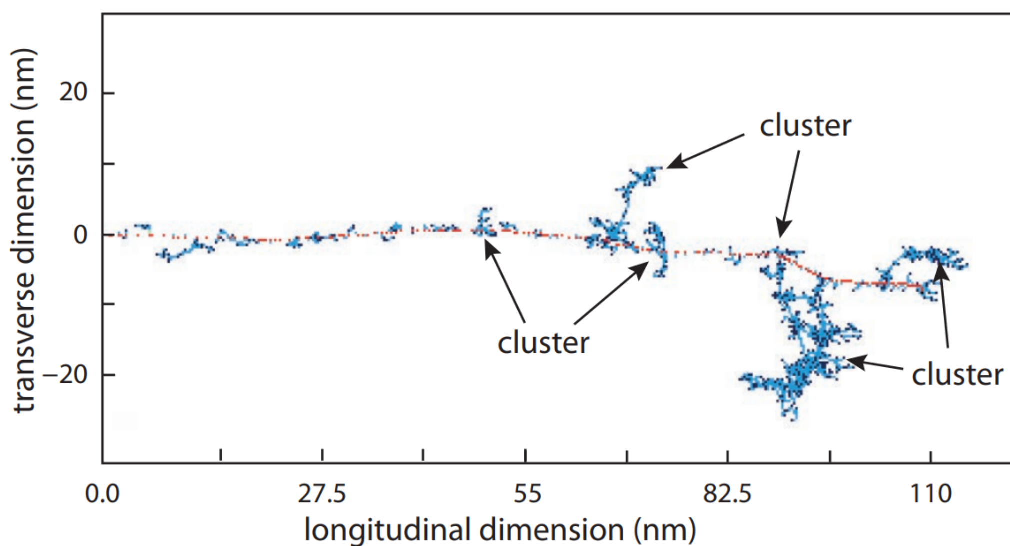


Figure 4.8.: Simulated Si lattice damage for a typical 1 MeV neutron recoil [46].

# 5. ATLAS ITk Pixel Detector

The ITk, a pivotal aspect in the entire HL-LHC upgrade, consists of more than 10,000 silicon Pixel Detector modules. There are different types of modules used in the various sections of the ITk, but the majority of the roughly 10,000 Pixel modules are planar quad modules, as illustrated in Figure 5.1. The name already implies that such modules feature 4 front-end chips (FE) per module. To allow high precision, each chip is segmented into 384 $\times$ 400 pixels, making a total number of 153,600 pixels. They comprise a hybrid design, which means that the sensor is directly connected to the readout electronics via small metal bump bonds [58]. In total, ITk Pixel will cover an active area of $\approx 13\,\text{m}^2$. This chapter is dedicated to the outer barrel ITk Pixel quad modules, which are investigated within the scope of this thesis.

## 5.1. Sensor

The Si sensor is the passive material part for the detection of particles. The sensors used in outer barrel ITk Pixel are $150\,\mu\text{m}$ thick. The ITk Pixel sensors are segmented into pixels with a pixel pitch of $25 \times 100\,\mu\text{m}^2$ in the innermost barrel layer and $50 \times 50\,\mu\text{m}^2$ elsewhere in the ITk. Most of the sensors are planar sensors, of nearly $4 \times 4\,\text{cm}^2$ dimension. The central interchip region features larger pixel of $50 \times 100\,\mu\text{m}^2$ or $100 \times 100\,\mu\text{m}^2$ dimension to allow for interchip margin. High voltage (HV) can be applied to the sensor for biasing.

## 5.2. The ITkPixV2 Readout Chip

The latest version of the readout chip for the ITk is the ITkPixV2, which is the ATLAS-specific implementation based on the RD53C [59]. This chip is designed to meet the requirements of radiation hardness and readout speed. The chip's technology is based on CMOS implemented logic elements. The chip has an analogue as well as a digital part of the circuitry. The chip reads out the 384 $\times$ 400 pixels, so in total nearly 615,000 pixels are connected to a single module. One of the new and advanced technologies that the ITkPixV2 will bring to the ITk is serial powering, which will reduce the number of power

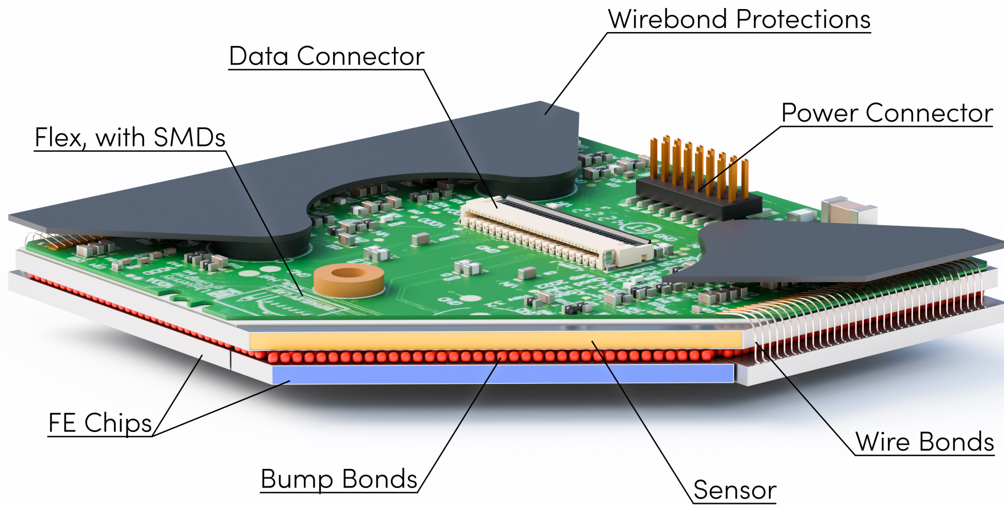


Figure 5.1.: Schematic of an ATLAS ITk Pixel quad module, showing the different layers and components (not to scale). The Figure was created using the CAD model from [57].

cables inside the detectors. The foundation of the serial powering is a custom constant current regulator, the SLDO ( =Shunt linear Low Drop-Out) [60]. The chip distributes the input current $I_{\text{in}}$ to the core current, so the current $I_{\text{core}}$ that is actually consumed by the circuit and the shunt current $I_{\text{shunt}}$, which compensates for power consumption fluctuation such that $I_{\text{in}} = I_{\text{core}} + I_{\text{shunt}}$. The ultimate goal is to operate multiple devices connected simultaneously in constant current mode by redirecting additional current into the shunt circuit, which exists for both the digital and the analogue part of the circuitry.

The characterisation and investigation of the chips is a crucial aspect to secure a reliable operation of the ITk.

## 5.3. Bare Module

The pixelated sensor and front-end chip are interconnected with metal bump bonds to form a Bare Module (BM), which is a characteristic of hybrid Pixel Detectors. The bump bonding process, which is a crucial step in the fabrication process of the ITk modules, is done by different industrial vendors.

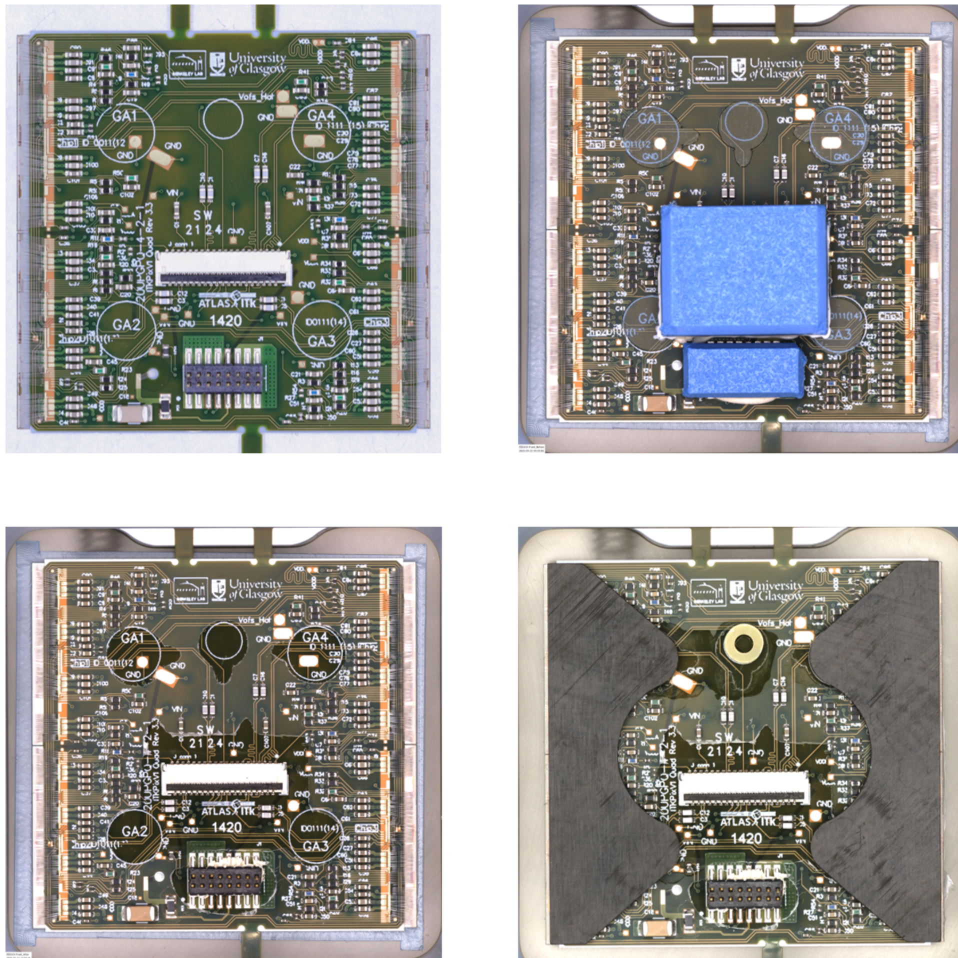


Figure 5.2.: One production module at different stages of the production cycle: on the top left: the module after wirebonding, in the top right: fully masked, ready for coating, on the bottom left: demasked and parylene coated, and on the bottom right: with Carbon canopies and strain relief.

## 5.4. Flex

The flexible PCB (flex), with the surface-mounted devices (SMD), so the electrical components, such as transistors or resistors, mounted to the flex, is glued on top of the BM, and is interconnected via thin wires, the wire bonds. The wire bonds allow for data and power connection with the chips. As shown in Figure 5.2, there are two connectors on the flex. The power connector is for biasing the sensor with HV for full depletion, low voltage (LV) for operation of the chips and also the Negative Temperature Coefficient Thermistor (NTC) readout. Flat ribbon cables, called pigtails, are attached to the connectors. There are 4 circular areas on the flex which are free of any SMDs. Two of these pickup points feature a ground pad. The pillars of Carbon canopies are glued onto these areas.

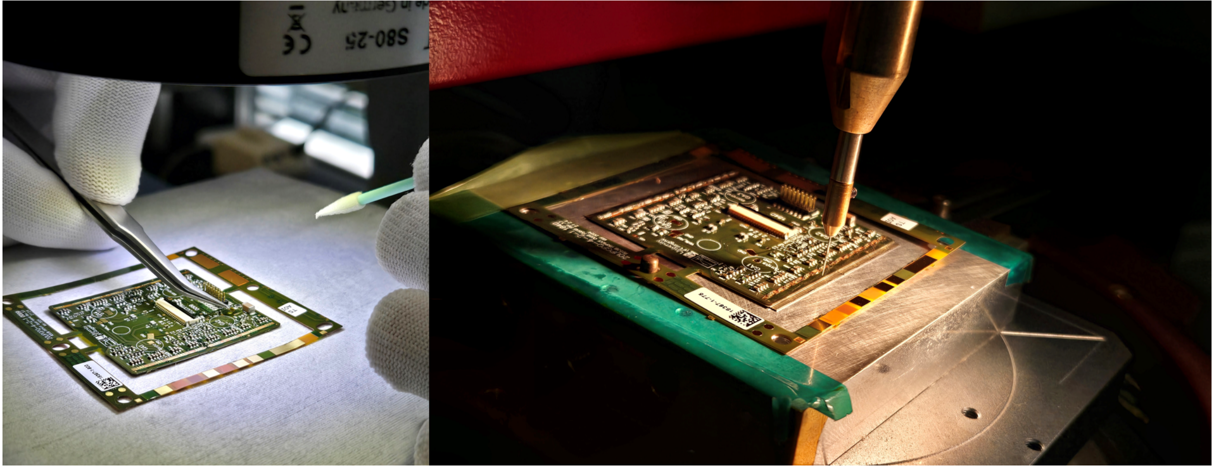

Figure 5.3.: Insights into the ITk Pixel module production for the German cluster at FTD in Bonn. On the left, one can see the precise positioning of Kapton stickers to cover the hole in the flex, which is essential to prevent any glue leakage into the hole dedicated to the HV wire bonds. On the right, a picture of the pull tester is shown (winner of the LHC-ErUM-FSP Photo Competition). Certain wire bonds are sacrificed for pull testing to monitor and secure strong wire bonding quality.

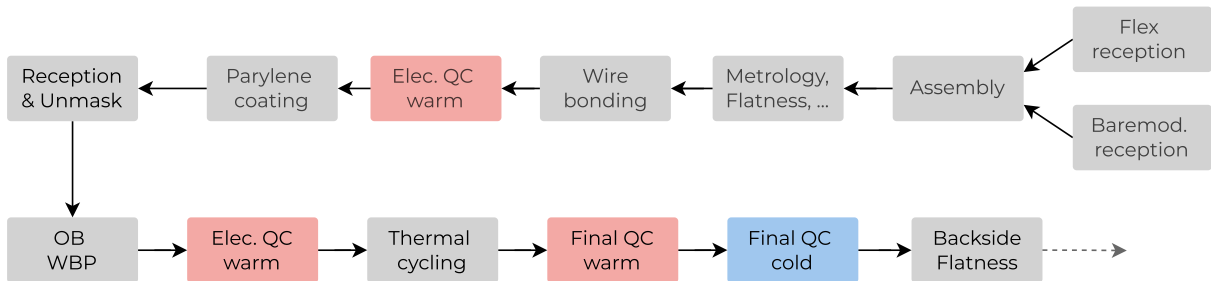


Figure 5.4.: Pixel module production flow chart.

## 5.5. Assembly

The production of ATLAS ITk Pixel modules comprises a multi-step procedure, illustrated in Figure 5.4. The highly delocalised production, including assembly and testing, is distributed worldwide.

In a first step, metrology of the two main components, the BM and the flex, is performed. Within the scope of the metrology, the mass and dimensions of the BM or flex are determined and documented. Additionally, each component is photographed. Next, the BM and the flex are glued together with the help of the $\mu$m-precision gluing tools. The glued module undergoes metrology after the gluing. Next, the Flex and the readout chips are interconnected with fine wires in the wire-bonding process. This filigree task is accom-

plished with the help of (semi-) automatic bonders. Certain wire bonds are bonded with the sole purpose of being pulled afterwards using the pull-tester. The pull-tester, shown in Figure 5.3, determines the bonding strength and monitors the bonding quality. Hereafter, certain crucial areas, such as the pickup points and the connectors of the modules, are masked with a sticky blue tape. On top of that, the power and data adapter are covered with 3-D-printed lids, further protected with Stannol. The Stannol is a peelable masking compound used in electronics assembly. It is a latex-like, room-temperature–curing "peelable solder masks" designed to temporarily protect selected areas from glues, encapsulants, conformal coatings, solder, or dust. The masking step prepares the modules for parylene coating. The parylene, which serves as an insulator between the strongly biased sensor and the delicate chips, is applied in a multi-hour coating process either by the company APS in Paris, France or by the Max-Planck-Institute for Physics (MPP) in Munich. The few $\mu$m of parylene, which also covers the fragile wire bonds, also enhances their bonding strength, resulting in more robust wire bonds. Back at the institutes, the coated modules are demasked, meaning the sensitive areas, which were covered with blue tape during coating, are uncovered. During the process step of demasking, the Stannol masking is removed mechanically by peeling, leaving the protected surfaces clean and ready for electrical contact or metrology. Lastly, the Outer Barrel Wire-Bond Protections (OBWBP), the small carbon canopies are glued onto the modules, using the precise OBWBP glueing tools. Furthermore, a circular strain relief is glued to the flex in this assembly step. It helps with the redirected pigtails in cell loading, as shown in Figure 5.5.

A detailed assembly and production guide, which was developed within the scope of this thesis, can be found in the Appendix A.

## 5.6. YARR

YARR („Yet Another Rapid Readout") is the readout system used for chip communication [61]. A DisplayPort cable connects the chip to the PCIe-based readout system. The YARR readout system is used to operate and configure the chips and also to perform essential scans, which are part of the QC process.

**For the digital scan,** a definable number of triggers is sent to the digital part of the chip circuit several times. The chip's occupancy and the hit counts are observed. Ideally, all pixels should see every injected trigger pulse.

**The analogue scan** injects a certain charge into the analogue domain of the chip and tracks the chip's response. Unlike the digital scan, the analogue part of the chip is subject to noise. Therefore, the analogue scan is more likely to show deviations from the injected number of pulses.

**The Threshold Tuning** adjusts the global or pixel threshold value. A desired charge is injected into the analogue circuit, and a global or pixel chip threshold parameter (Vth1) is altered until half of all pixels register a hit.

**The Threshold Scan** measures the distribution of the pixel threshold values. A range of increasing charges is repeatedly injected into each pixel. The pixel's response is measured. The threshold is defined as the 50% occupancy point for each pixel.

**The ToT scan** determines the Time over Threshold for a particular injected charge, typically 6000 e.

**The Noise scan** detects and masks noisy pixels. Some pixels show many more hits than the natural electronic noise could have produced, and spoil the tests.

**Merged & Disconnected bump scan** use pixel cross-talk effects to detect disconnected or merged bump bonds. To locate such bump bonds, the influence signal of a particular pixel is analysed if charge is injected into surrounding pixels.

## 5.7. Pixel Performance Tests

The pixel performance tests are performed on the modules after canopy attachment and within the scope of final QC. There are 3 test steps in the Pixel Performance Tests.

**The Minimum Health Test** (MHT) checks the FEs functionality. The MHT comprises a digital scan, an analogue scan, a threshold scan and a ToT scan.

**Tuning** the discriminators' reference voltage influences the detector's sensitivity and will be done regularly during operation.
The tuning comprises a first threshold scan (before the tuning process), a global threshold tuning, followed by a pixel threshold tuning and lastly a threshold scan and a Tot scan after tuning.

The tuning is successful if the mean threshold after tuning is within 100 e around the targeted value with a noise of less than 50 e.

**The Pixel Failure Analysis** (PFA) verifies the final performance of a detector module. The PFA comprises: a digital scan, an analogue scan, a threshold scan, a noise scan, a disconnected- and a merged bump scan, optionally concluded by a self-trigger source scan. Overall, the PFA creates the mask of pixels that are excluded, for example, because they are noisy or do not meet the specifications otherwise. In the final cold stage, the detector modules are probed with real ionising radiation using a $\beta^-$-source in the new QC-box, further treated in [62], using the self-trigger source scan.

**Thermal Cycling** To certify that the Pixel Detector modules can survive the large temperature differences they face during regular operation for years, they are thermal-cycled before proceeding to the final QC [59].

## 5.8. Local & Production Database

To track the achievements and the steps performed at the different institutes, the QC test results, the components metrology and the configuration files are uploaded to a central Production Database (PDB) [63]. In a first step, the test results are uploaded and analysed in a Local Database (LocalDB), which acts as an interstage between the local QC testing and the PDB.

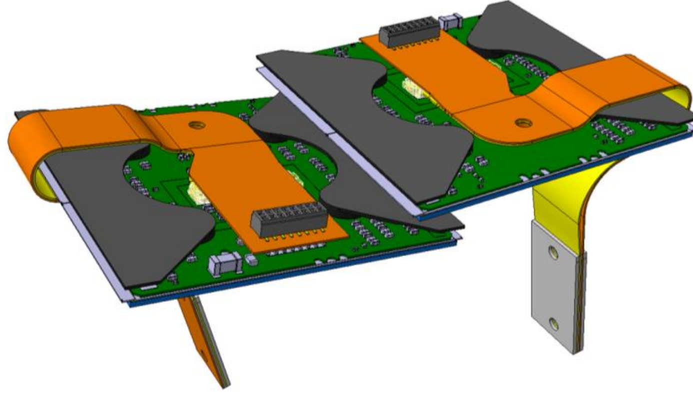

Figure 5.5.: Schematic of outer barrel quad modules on LLS [64].

## 5.9. Cell Loading

Each module that successfully passes the QC chain qualifies for installation onto a Carbon-made loaded local support structure (LLS) [64]. Therefore, the modules are glued to a Carbon cell, which secures thermal contact. The cell loading demands the module's backside to meet precise flatness criteria, which is checked with the backside flatness measurement.

For cell loading, the modules are fitted with folded, origami-style pigtails, as illustrated in Fig. 5.5. This routing is mandated by the tight layout and strict detector-envelope tolerances in the outer barrel: there is no straight path for the flex tails that satisfies the available clearances and connector positions. Folding the pigtails keeps the services within the allowed radial and lateral envelope and avoids clashes with neighbouring structures. Because the folded tails run close to the exposed wire-bond rows, an Outer-Barrel wire-bond-protection (OBWBP) scheme is implemented to safeguard the bonds during handling and installation.

# 6. The SLDO Scan and the Mirror Current Factors

The ATLAS ITk will feature a novel serial powering which reduces the number of cables within the detector and therefore has a positive impact on reducing the material budget. A demonstrator of such a serial power chain is shown in Figure 6.1. The foundation of the serial powering is a custom constant current regulator called Shunt Low Drop-Out regulator (SLDO), which combines the linear Low Drop-Out (LDO), in Figure 6.2 in red, with a shunt element in Figure 6.2 in black. The goal of the SLDO and the serial powering is to provide constant current operation with multiple devices (Pixel Detectors) connected simultaneously. Since the shunt circuit compensates for power consumption fluctuations of the single Pixel modules as shown in Figure 6.3, the SLDO acts as a dynamic current buffer. The additional current in the circuit is redirected into the shunt circuit. There is a shunt circuit and therefore a shunt current in both the digital and analogue part of the chip's circuit.

On a quad module, there are 4 ITkPixV2 FE chips, which are powered in parallel. Therefore, it is not possible to directly access the currents or voltages to individual chips or rails. Measurements rely on the multiplexer (mux) to read on-chip current and voltage.

For testing, one can use a single chip card, with only one ITkPixV2 FE chip. Using a single chip card, it is possible to directly power the chip and measure the current and voltage, such that this setup can compare on-chip (mux) measurements to direct measurements. On a single chip card, it is possible to switch manually between the LDO and SLDO mode using a jumper as shown in Figure 6.6. The modules are powered by an external power supply, which provides the input current $I_{\text{in}}$. This current $I_{\text{in}}$ is then split into the core current $I_{core}$ (Figure 6.3 in blue) consumed by the chip and the shunt current $I_{\text{shunt}}$ (Figure 6.3 in yellow), such that: $I_{\text{in}} = I_{\text{core}} + I_{\text{shunt}}$.

Since the SLDO and serial powering are essential for stable detector operation, their performance must be evaluated during module quality control (QC).

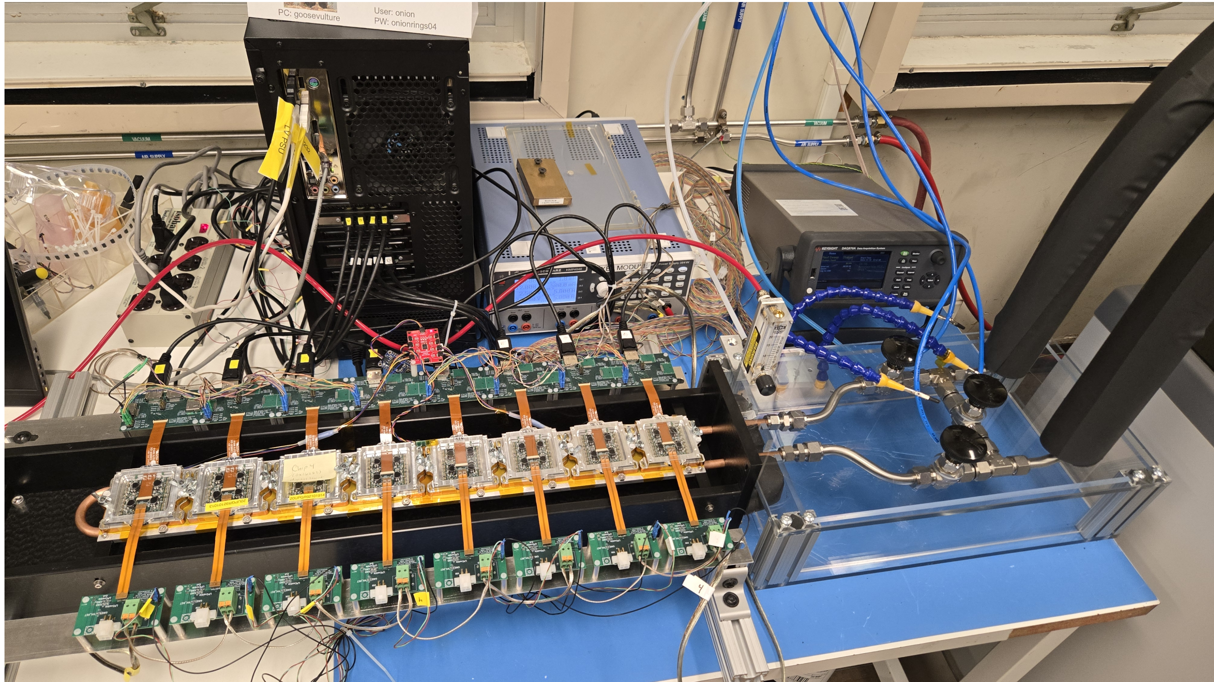


Figure 6.1.: Demonstrator of a module serial power chain with 8 ATLAS ITk Pixel modules connected simultaneously at the LBNL.

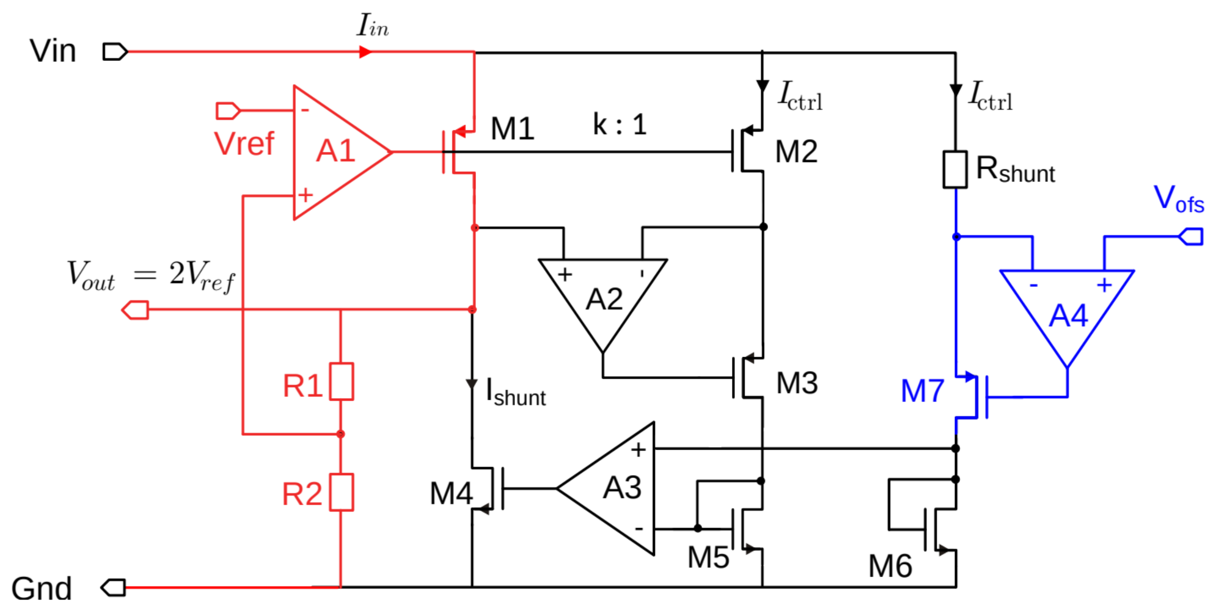


Figure 6.2.: Simplified schematic of the RD53C SLDO regulator. The colours differentiate the LDO (red), shunt (black), and offset (blue) part of the circuit [59].

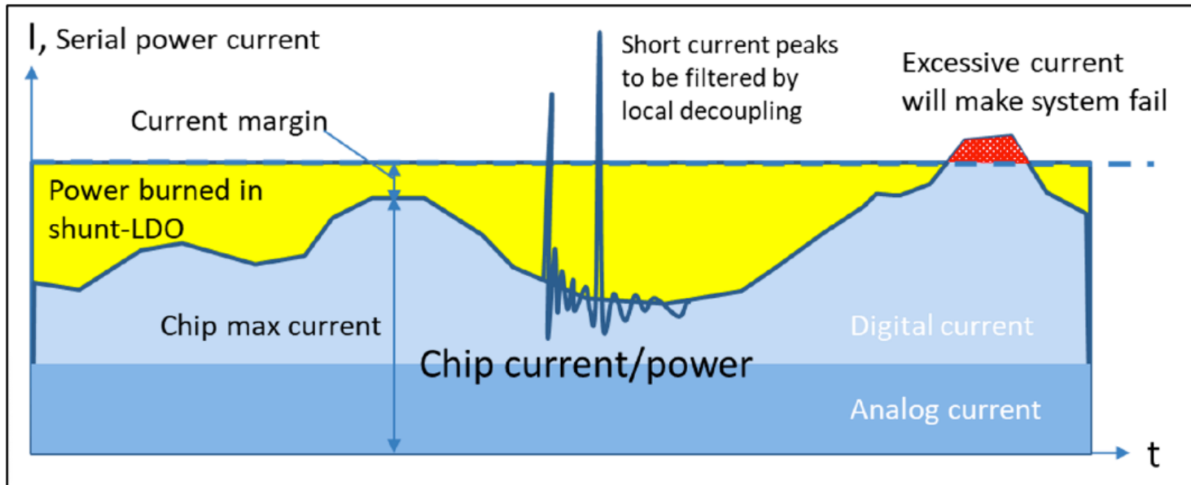


Figure 6.3.: Schematic current distribution in an ITk Pixel module. The red region, the so-called undershunted case, should be avoided.

## 6.1. The SLDO Scan

The SLDO analysis probes several chip internal currents and voltages, such as the shunt current $I_{\text{shunt}}$ or the input current $I_{\text{in}}$. Both shunt currents, the digital and the analogue ones, are probed for different currents provided by the power supply $I_{\text{PS}}$. The power supply current is ramped down from 7.55 A to 5.55 A. Since a linear behaviour is expected between the power supply current and the shunt current, a linear fit is performed with a dynamic fitting range. The chip does not show proper functionality, if the shunt current is too small, this case is called undershunted (see Figure 6.3 in red). This case must be avoided under all circumstances, to secure minimal chip currents for working operatively. Also, the shunt current is unstable when it is too low, so close to the undershunted case. On the other end, large shunt currents were observed to cause loss of communication with the chips. That is also the reason why the SLDO analysis was changed during production, and the maximal current provided by the power supply was reduced to a maximal value of 7.55 A. For this reason, a trustworthy region of shunt currents is defined to be above 50 mA shunt current. The last 4 shunt current values above 50 mA are taken into account for the linear fit. The fit also takes special cases, such as loss of communication, into account. There are shunt current cut criteria which mark the minimal required shunt current. For the digital shunt current this criterion is 0.125 A and for the analogue shunt current it is 0.006 A, as shown in Figure 6.4 on the left. The dynamic fit extrapolates the minimal power supply input current such that the shunt current cut criteria are met.

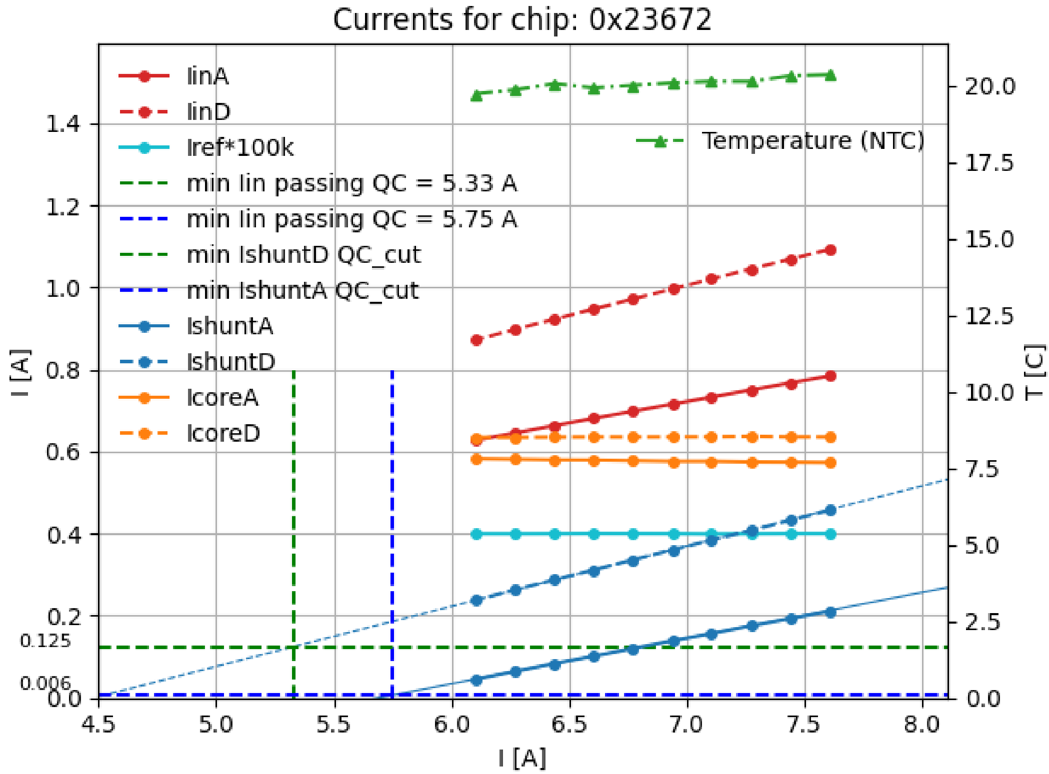


Figure 6.4.: Scan output of the SLDO analysis. The different internal currents such as $I_{\text{shunt}}$ are plotted against the power supply current.

These two points of interest are put out and are also graphically displayed as shown in Figure 6.4 with the dotted lines and the legend. An error statement is included in case there are not enough points in the trustworthy region of above 50 mA shunt current.
A $\chi^2$ test quantifies the fit quality. In the end, the measured data is uploaded to the PDB.

## 6.2. Mirror Current Factor

The chip exhibits shunt current in both the analogue and digital circuits. In addition to reading out the current for the purpose of testing and verification of the SLDO, the chip's internal currents are also mirrored at certain points of the circuit. Combinations of transistors act as current mirrors as shown in Figure 6.5. The current mirrors amplify the mirrored current by a factor $k$, which is the ratio between the actual current and the current read from the chip's mux. The ratio is also included in the schematic in Figure 6.5. The expected total amplification factor is the product of all transistor ratios.

Due to the amplification by the factor $k$ of the mux current compared to the actual current: $I_{\text{actual}} = I_{\text{mux}} \cdot k$, the mirror current amplification factors are also referred to as $k$-factors. In theory, these $k$-factors should only depend on the transistor's geometry. In practice, the $k$-values are influenced by multiple parameters such as process variations, temperature, supply voltage and local biasing or the operating mode (LDO or SLDO). There are different ways to access these $k$-factors. The current factors of interest in the chips are the ratio between the current from the multiplexer, $I_{\text{mux}}$, read within the chip and the power supply current, $I_{\text{PS}}$. The current $I_{\text{mux}}$ can be accessed with a single chip card, which has numerous external resistors $R_{\text{ext}}$ installed on it.

There was limited knowledge of the actual $k$-factors and how they differ from the assumed default ones and from those recorded during wafer probing. Moreover, the stability of these current amplifications over different temperatures that could be reached in operation was unexplored before. Also, the $k$-factors recorded during wafer probing are determined at a temperature different from the one during operation and the one in warm probing. Prior measurements of related factors were only done with previous chip versions and had not been repeated with the final chip version. The ultimate goal is to understand the $k$-factors, their behaviour and the dependences.

To systematically probe the $k$-factors, a script is written to loop over different pre-amplification and core column settings because the pre-amplification (preamp) controls the analogue circuit and the number of enabled core columns (corecols) addresses the

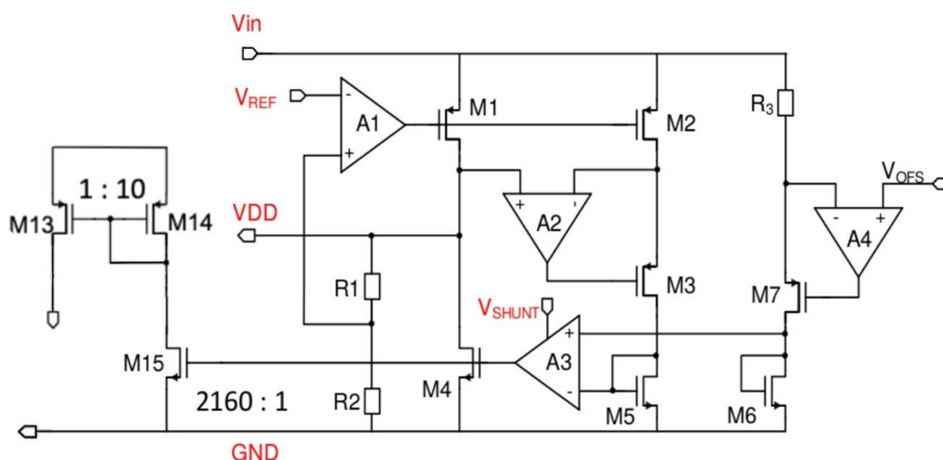


Figure 6.5.: Section of the schematic under-shunt protection circuit. The amplification and mirror of the shunt currents in the circuit via a combination of transistors are marked [59].

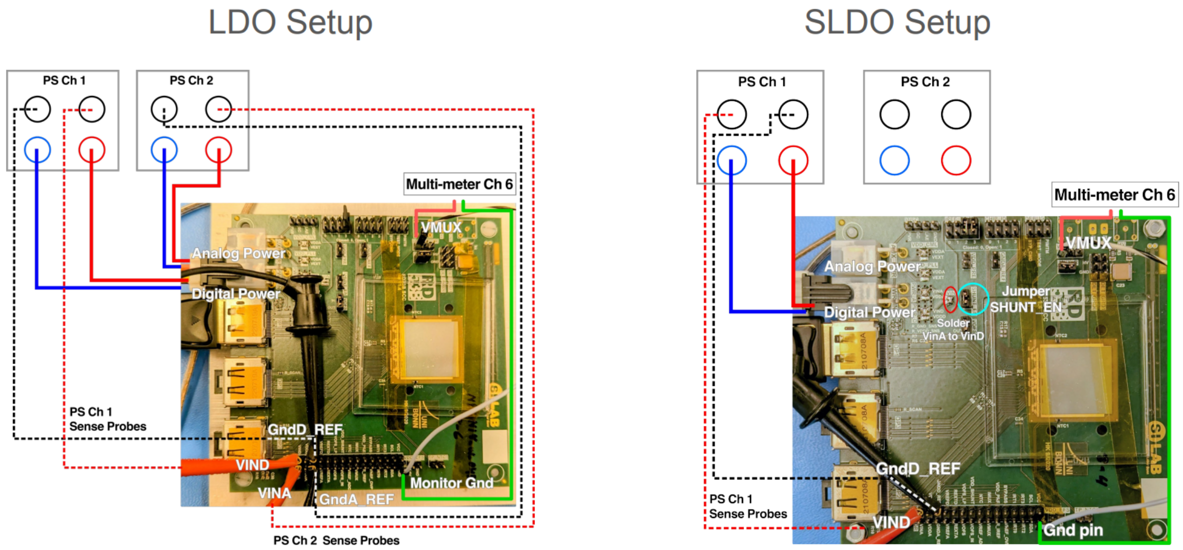


Figure 6.6.: Single Chip Card setup with sense wires in LDO mode and SLDO mode ©Maria Satnik/Berkeley Lab.

digital part of the circuit. The data is stored in a dictionary. At first, also cross terms are included to test if the per se independent circuits influence each other. Since the independence of the two circuits is observed with the first measurements, the cross terms were excluded from the following measurement and script versions.

Starting in LDO mode, the digital and analogue circuits are powered with different channels on the same power supply, as shown in Figure 6.6. The first two $k$-factors are found here in LDO mode, as the slope of the linear fit between the input current from the mux $I_{\mathrm{in}_{\mathrm{A/D}}}$ and the power supply current $I_{\mathrm{PS}}$. These two are referred to as $k_{\mathrm{in}_{\mathrm{A}}}$ and $k_{\mathrm{in}_{\mathrm{D}}}$.

Next, the chip is switched into SLDO mode by manually entering the jumper on the single chip card. The jumper connects or disconnects the shunt element from the LDO circuit, such that it is possible to switch between LDO and SLDO mode. Moreover, the analogue and digital power cables are connected to the same power supply channel as shown in Figure 6.6 on the right. In SLDO mode, the shunt current according to the power supply and the shunt current read from the mux are directly proportional. The ratios of these two currents are the remaining two $k$-factors, named $k_{\mathrm{shunt}_{\mathrm{A}}}$ and $k_{\mathrm{shunt}_{\mathrm{D}}}$. In total, there are 4 mirror current factors: $k_{\mathrm{in}_{\mathrm{D}}}$, $k_{\mathrm{in}_{\mathrm{A}}}$, $k_{\mathrm{shunt}_{\mathrm{A}}}$ and $k_{\mathrm{shunt}_{\mathrm{D}}}$, from which two are determined in LDO mode, and using the SLDO mode, the other two are determined.

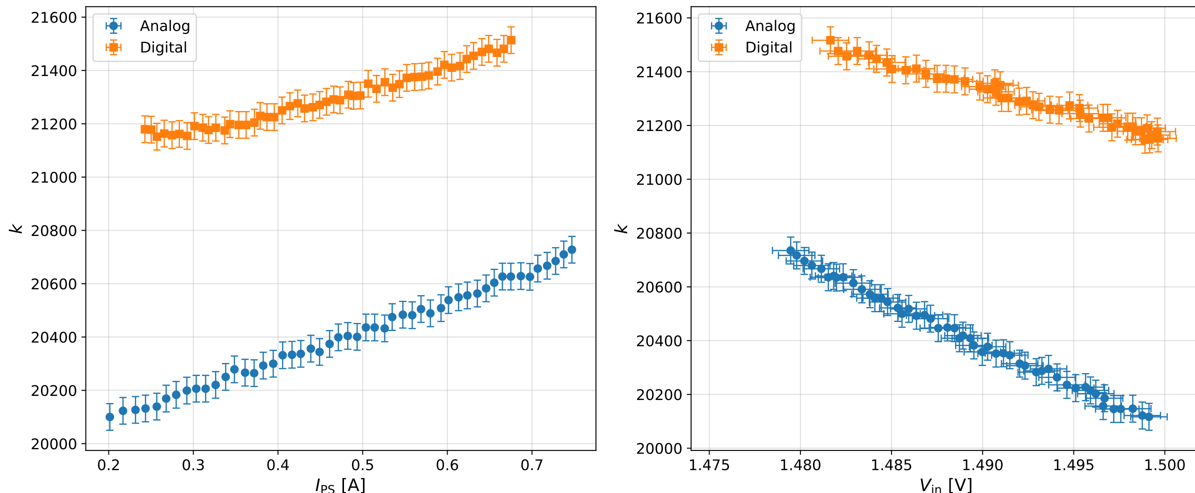


Figure 6.7.: $k$-factor measurements in LDO mode. For the $k$-values an uncertainty of $\sigma_k$=50 is assumed, the power supply has an uncertainty of $\sigma_I = 1\,\mathrm{mA/mV}$.

Firstly, the plots in Figure 6.7 show the results of the digital and analogue $k_{\mathrm{in}}$-factors measurement plotted against the power supply current $I_{\mathrm{PS}}$, on the left, as well as the $k$-factors plotted against the voltage provided by the power supply, on the right. A first observation is, that there is an effect from the small input voltage changes. The $k$-values changes about 330 per 10 mV input voltage change. On top of that, the $k_{\mathrm{in}}$ show an increase of roughly 0.5% per 100 mA power supply current increase. The behaviour of the $k$-factors increasing means that the current read from the chip mux $I_{\mathrm{mux}}$ is getting smaller than the power supply current $I_{\mathrm{PS}}$.

Next, the resulting shunt current in SLDO mode according to the power supply $I_{\mathrm{shunt_{PS}}}$ is calculated according to Equation 6.1 [59]:

$$I_{\mathrm{shunt_{PS}}} = I_{\mathrm{PS_{SLDO}}} \cdot \underbrace{\frac{R_{\mathrm{ext_{A/D}}}}{R_{\mathrm{ext_A}} + R_{\mathrm{ext_D}}}}_{\approx \frac{1}{2}} - I_{\mathrm{PS_{LDO}}}. \tag{6.1}$$

The power supply shunt current $I_{\mathrm{shunt_{PS}}}$ depends on the external resistors $R_{\mathrm{A}}$ for the analogue circuit, and $R_{\mathrm{D}}$ for the digital one. Initially, these two were measured to be the same within the measurement uncertainties, such that the ratio is approximately $\frac{1}{2}$. The calculated shunt current from the power supply is directly proportional to the shunt current according to the mux of the chip: $I_{\mathrm{shunt_{PS}}} = k_{\mathrm{shunt}} \cdot I_{\mathrm{shunt_{mux}}}$, where the proportionality factor is the $k_{\mathrm{shunt}}$ factor.

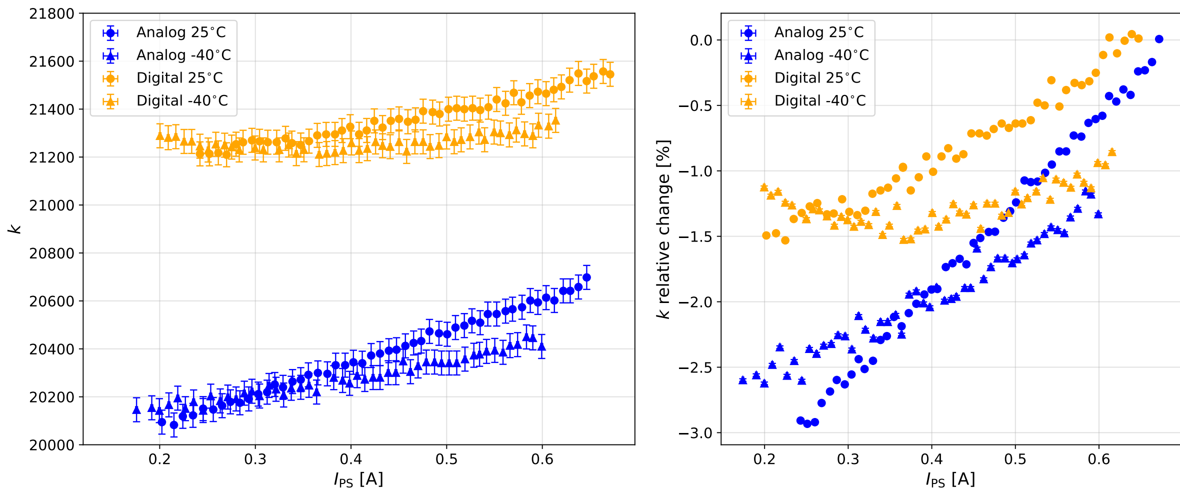


Figure 6.8.: Final mirror current amplification factors in LDO mode. For the $k$-factors, an uncertainty of $\sigma_k = 50$ is assumed.

To access the full shunt current regime, the external resistors on the single chip card are replaced with higher ohmic resistors.
Additionally, sense wires are installed on the power supply to compensate for the voltage drop over the cables. Figure 6.6 shows the final setups.

The resulting final $k-$factor measurements are shown in Figure 6.8-6.10. The average value depicted in the legend is the average of all measured values in the stable shunt current regime above 125 mA. Additionally, the measurements were repeated in a climate chamber to determine the temperature dependence of the $k$-factors.

Figure 6.8 on the left shows the $k_{\text{in}}$-factors in LDO mode plotted against the power supply current. The $k$-factor values for the digital circuit are higher than the analogue ones. The measurements for the maximal and minimal temperature, at which the measurements are repeated, agree within 3% as the right plot in Figure 6.8 shows. In this plot, the percentage change in the k-factors relative to the value measured at the highest power supply current in the warm state is shown.

The left plot in Figure 6.9 shows the $k_{\text{shunt}}$-factors plotted against the power supply shunt current. Again one can observe, that generally the digital shunt current factors are higher than the analogue ones. Furthermore, the measurements and the average values at the extreme measurement temperatures of +25 °C and -40 °C agree with each other within 1%. This shows the temperature stability that was hoped to be confirmed. In this lower shunt current regime, the highly non-linear behaviour is observed, which results

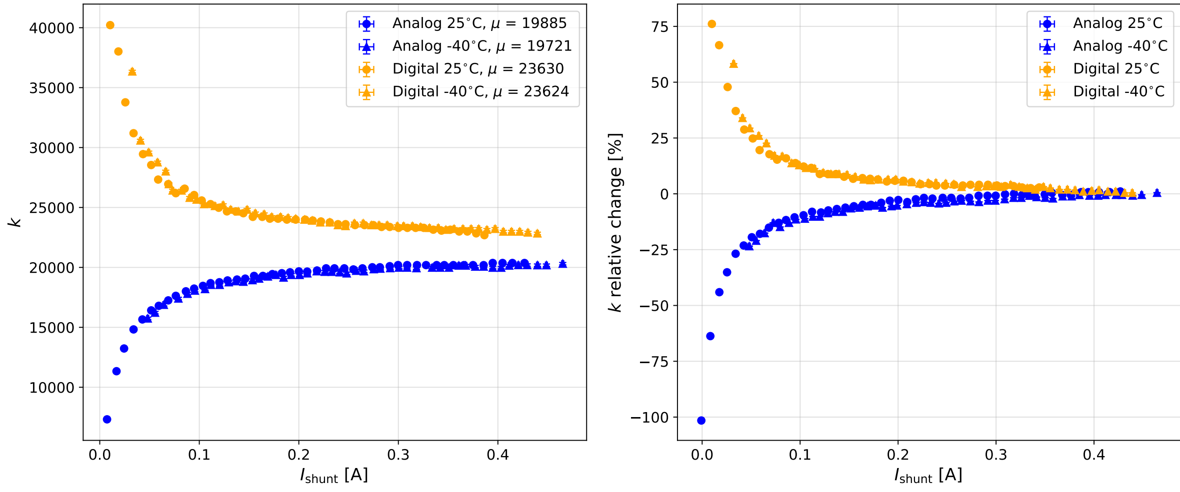


Figure 6.9.: Final results in SLDO mode. Since the shunt current shows more fluctuations, an uncertainty of $\sigma_k = 100$ is assumed.

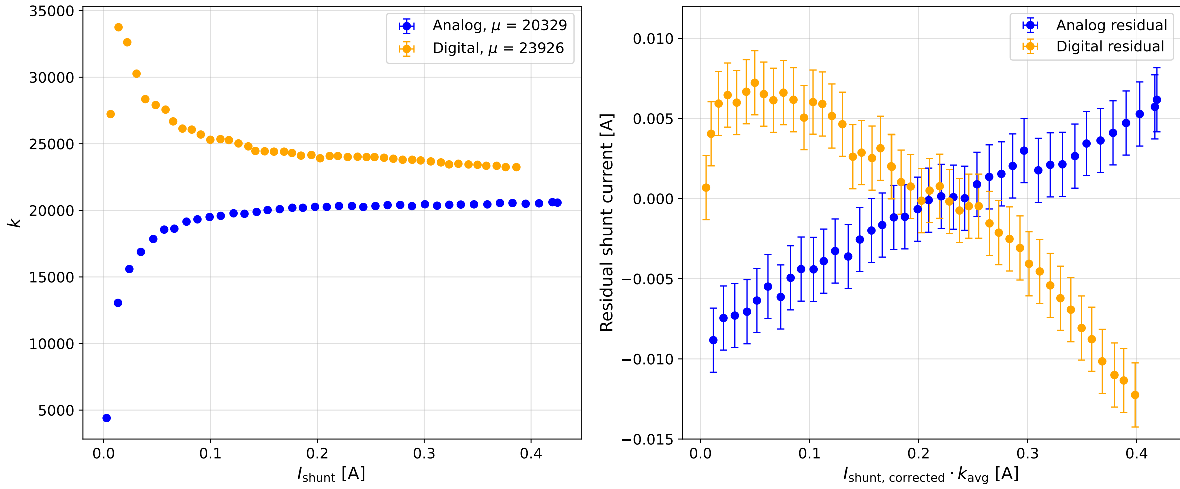


Figure 6.10.: Final results in SLDO mode with residual current. Again, $\sigma_k$ is assumed to be 100. The residual current is assumed to have an uncertainty of 2 mA.

from the calculation of the $k_{\text{shunt}}$-factors as a fraction of $\frac{I_{\text{shunt}_{\text{mux}}}}{I_{\text{shunt}_{\text{PS}}}}$ and since the denominator approaches zero, the $\frac{1}{x}$-like behaviour is observed. The observed behaviour arises independently of the temperature.
The right plot in Figure 6.9 shows the percentage change of the $k_{\text{shunt}}$-factors relative the measurement point with the largest shunt current. Again, just a small deviation between the different measurement temperatures is observed which demonstrated the temperature stability also in SLDO mode.

Since the temperature dependency was observed to be in the order of one percent, the final measurements are only conducted at warm.
The plots in Figure 6.10 show another measurement series of the $k_{\text{shunt}}$-factors plotted against the power supply. The average $k$-factors above 125 mA shunt current is displayed in the legend in the left plot. The right plot in Figure 6.10 shows the residual shunt current, so the difference between the shunt current according to the power supply and the shunt current according to the chip's mux corrected by the average $k_{\text{shunt}}$-factors: $I_{residual} = I_{\text{shunt}_{\text{PS}}} - I_{\text{shunt}_{\text{mux}}} \cdot k_{shunt_{avg.}}$, plotted against the shunt current from the mux calculated using the average $k_{\text{shunt}}$-factors from the left plot: $I_{\text{shunt}_{\text{mux}}} \cdot k_{shunt_{avg.}}$. In theory, if the $k$-factors were constant with ideal values, this plot would show a parallel to the x-axis at zero. In reality, the plot shows that both circuits are not zero nor constant. It is remarkable that the analogue and digital $k$-factors behave inversely to each other.
It is also possible to manually calibrate the value of the $k$-factors and then correct for the offset in the residual current plot such that the residual shunt current is nearly constant, meaning that the power supply and the module mux current agree. This way, the ideal behaviour can be approached as shown in Figure 6.11. Since the sense wire guarantees the current and voltage input into the chip, minimising the residual shunt current can be another ways to determine the actual $k$-factors of the chips.

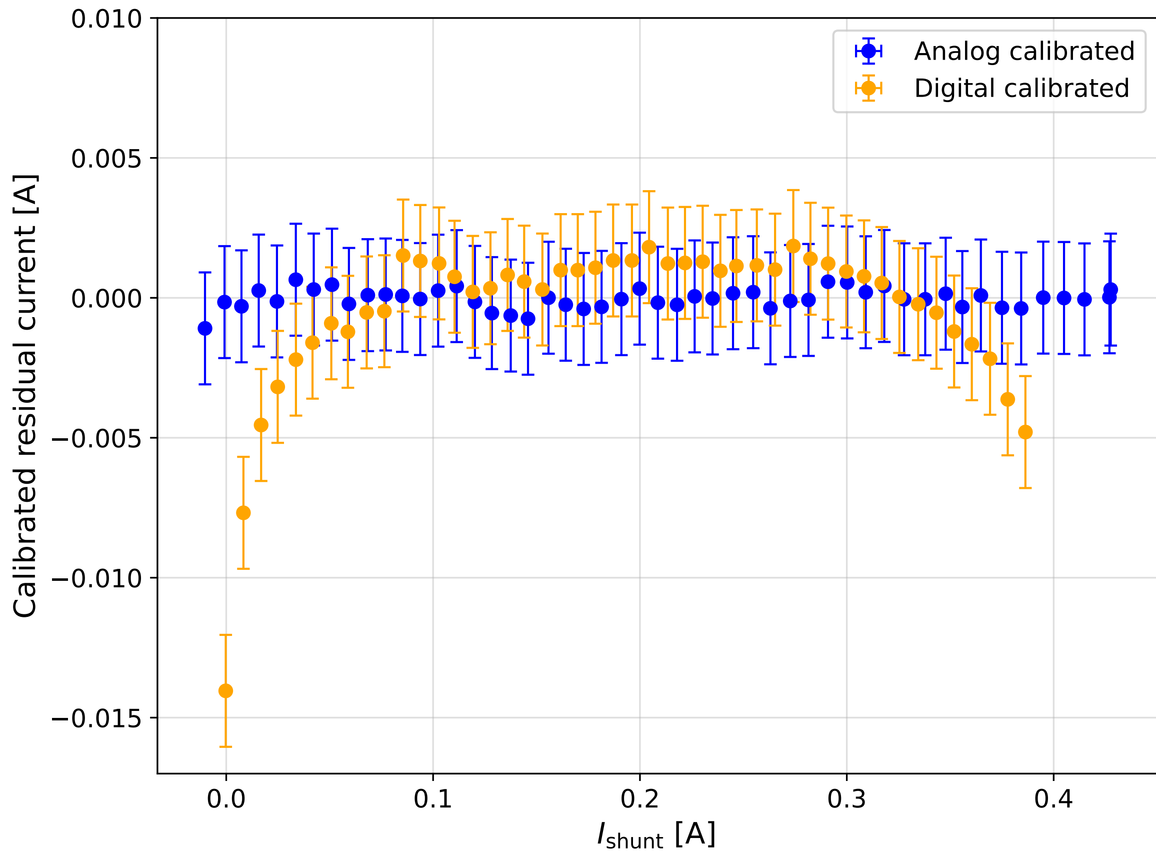


Figure 6.11.: Manually calibrated $k$-factors such that the residual current is nearly constant and then corrected for the offset. Again, the residual current is assumed to have an uncertainty of 2 mA.

# 7. Assembly Analysis

The delocalised production of the ITk Pixel modules is structured into national clusters. The German cluster will, in sum, produce roughly 1900 Pixel modules. The German cluster comprises the Rhenish Friedrich Wilhelm University of Bonn, the Georg-August-University of Göttingen and the University of Siegen, and the Max Planck Institute for Physics (MPP) in Munich is associated.

To secure a similar production standard and quality, detailed procedures are followed at all production sites. The procedures include the usage of specialised sub-$\mu$m precision tooling for assembly and gluing, and metrology. Since Bonn and Göttingen jointly organised their production, the majority of the Pixel modules produced within the German cluster are assembled in Bonn.

## 7.1. The FTD in Bonn

The FTD, the Research and Technology Centre for Detector Physics (German: Forschungs- und Technologiezentrum Detektorphysik), is part of the University of Bonn. The modern building features more than 3000 $m^2$ of technical infrastructure and laboratories dedicated to the development of modern detectors for experimental particle physics and beyond. The assembly is done as part of the ATLAS hardware team in the Working Group of Prof. Dr. Jochen Dingfelder. The delicate assembly procedure is conducted in the cleanroom facilities, which are located in the FTD building. There are several clean rooms with different ISO classifications at the FTD. The classification system is governed by the International Organisation for Standardisation (ISO) under ISO 14644-1, which defines cleanroom classes ranging from ISO 1 (most stringent) to ISO 9 (least stringent). Mostly, the assembly work is conducted in the ISO7 cleanroom. This cleanroom comprises assembly areas for gluing, an inspection station with sub-$\mu$m microscope, a wire bonder and a pulltester.

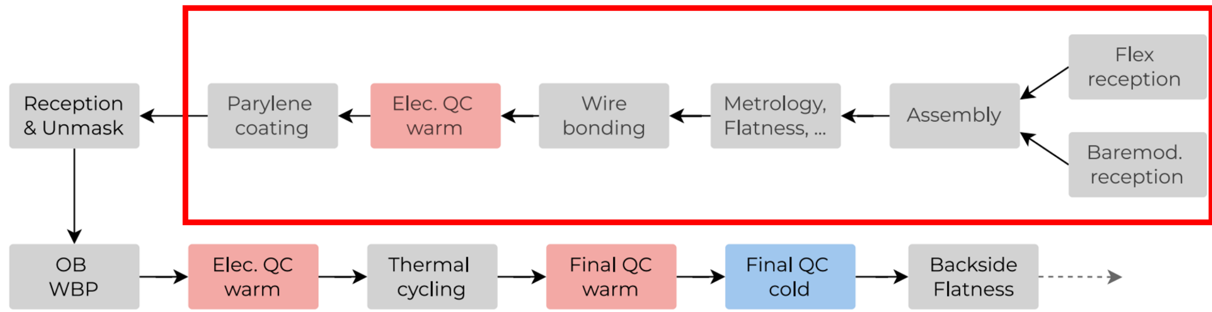


Figure 7.1.: Assembly chain for ATLAS ITk Pixel modules with the marked steps conducted at the FTD in Bonn.

The first half of the production steps, shown in Figure 7.1, are conducted at the FTD in Bonn, before the Pixel modules are sent to a company called *APS Coating* in Paris or the MPP in Munich for Parylene coating.

This chapter presents a statistical analysis of the first 322 Pixel production modules from the FTD in Bonn for the German cluster. Some measurements are performed at the chip level, while others were discontinued during the production process and are therefore not available for all modules, resulting in reduced statistics for certain observables.
The number of histogram bins is chosen according to the available data statistics. In most cases, the binning follows the Freedman–Diaconis rule [65]. However, when this rule yields fewer than 10 bins, a minimum of 10 bins is enforced. The mean and the standard deviation are calculated from the data sample. Most of the data is also used to perform a kernel density estimation (KDE).

## 7.2. Flex Reception

During flex reception, the flexible PCBs with the SMD components on top are inspected and measured in terms of their mass and dimension. In earlier production phases and pre-production, also the thickness was determined.
There are different types of flexes. The flex type is denoted with a flex serial number. For production only Outer System production flexes are used, which is represented by the number 4 in the flex serial number and in the module number, respectively. There are two different vendors producing such flexes, namely NCAB (serial number digit 2) and Tecnomec (serial number digit 8) [66]. Since the Tecnomec flexes are thinner and therefore lighter than the NCAB flexes, the mass distribution shown in Figure 7.2 exhibits two peaks, one around 1.8 g, and another peak at approximately 1.9 g.

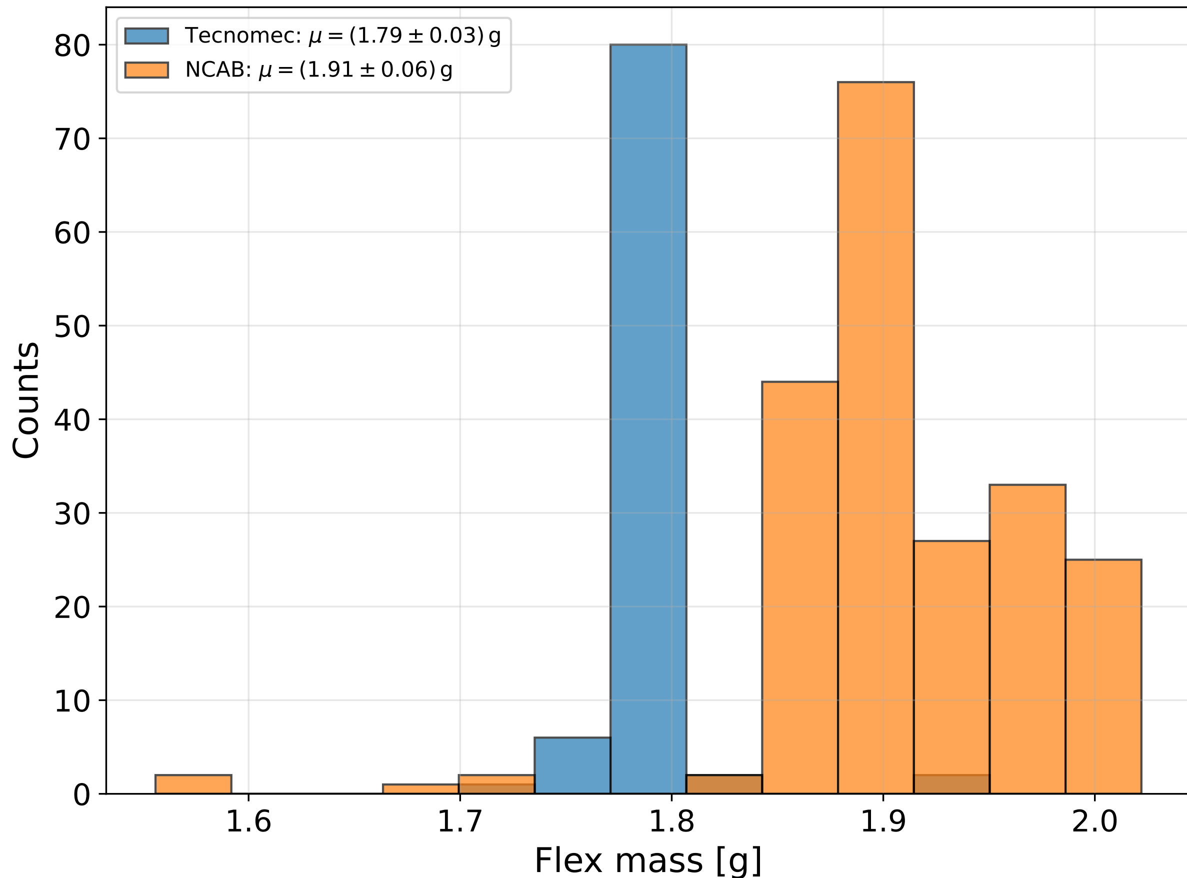


Figure 7.2.: Distribution of the flex masses, differentiated between the two vendors.

## 7.3. Bare Module Reception

Also, the BMs are received and tested at the FTD. They come from different external vendors which do the hybridisation, so the process of bump bonding, in which the small metal spheres melt the chip and the sensor together such that the bump bonding pattern matches the pixelation of the sensor doping.
In a first step of the reception, after photos are taken, the BM are probed in an IV-probe station. With the HV needles, the sensor behaviour is tested. Optimisations were done with the probe station at the FTD in Bonn. These optimisations include calibrating the adjustable positions of the probe station components, namely the microscope and the chuck (the base plate used for IV probing), as well as the precise positioning of the probe needles. In sum, the setup is improved towards a minimal number of manual interactions required to do the IV probing with this setup. The masses of the BM are determined during flex reception. In pre-production and earlier phases of production, also the BM thickness was determined, but these measurements were declared redundant.

Table 7.1.: Average glue mass and module thickness with standard deviation for each of the production tools. All values agree within $1\,\sigma$ of each other.

| Tool SN | Mean glue mass [mg] | Module thickness [$\mu$m] |
|---|---|---|
| 32 | $71 \pm 11$ | $644 \pm 16$ |
| 39 | $72 \pm 11$ | $641 \pm 11$ |
| 40 | $72 \pm 16$ | $636 \pm 21$ |
| 43 | $70 \pm 19$ | $638 \pm 11$ |
| 44 | $68 \pm 10$ | $640 \pm 14$ |
| 46 | $75 \pm 11$ | $636 \pm 12$ |

## 7.4. Gluing

As of today, 6 production tools are used at the FTD in Bonn. Located on the central workbench, the sub-$\mu$m precise alignment tools with the serial numbers 32, 39, 40, 43, 44 and 46 are used. The tooling is centrally provided to the production institutes around the globe. To test their compatibility with each other, one can look at certain parameters. Firstly, the glue masses all agree within $1\,\sigma$ between the tools as presented in Tab. 7.1.

There is a strict limitation on the module thickness because the available amount of space within the Inner Tracker is tightly packed and the spatial use is optimised in the best possible way, to fully exploit the potential of the ATLAS experiment.
The average module thickness of all so far produced modules is $(634 \pm 20)\,\mu$m as shown in the histogram in Figure 7.3, and all the tools agree within $1\,\sigma$ as presented in Tab.7.1. The distribution of module thicknesses lies well within the specified upper and lower thickness limits which are $510\,\mu$m and $750\,\mu$m, as also shown in the plot in Figure7.3.

A strict upper limit is imposed on the total module mass to ensure a reliable mechanical connection during cell loading and to prevent overloading of the local support structure. Consequently, the module mass must not exceed 3.5 g. So far, not a single assembled module was above this weight limit as shown in Figure 7.4.

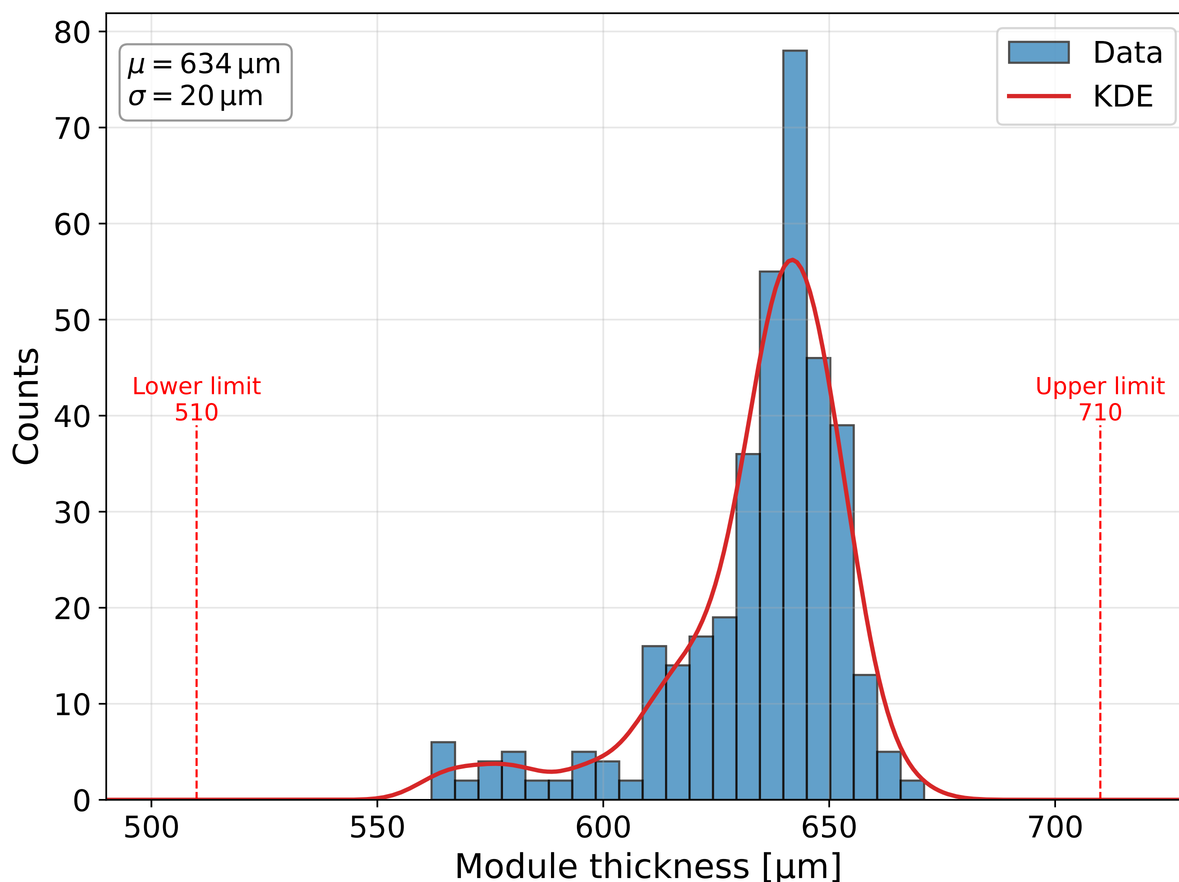


Figure 7.3.: Distribution of the module thicknesses with a kernel desity estimation (KDE) and limits.

To secure an even distribution of the applied glue and the subsequent flatness of the module, it is important to measure the thickness variation on the pickup points. The distribution of the maximal thickness variation between two pickup points on a module is plotted in Figure 7.5. Since the distribution is far below the 50 $\mu$m maximal thickness variation, also shown in the summary plot in Figure 7.9, this measurement was declared redundant and is no longer part of the module QC, which also explains the low statistics in Figure 7.5. The lower limit on the thickness variation arises naturally since a perfectly flat module would have a thickness variation of 0 $\mu$m. The measurements conducted during pre production and early production verify the stencil design in terms of even glue distribution.

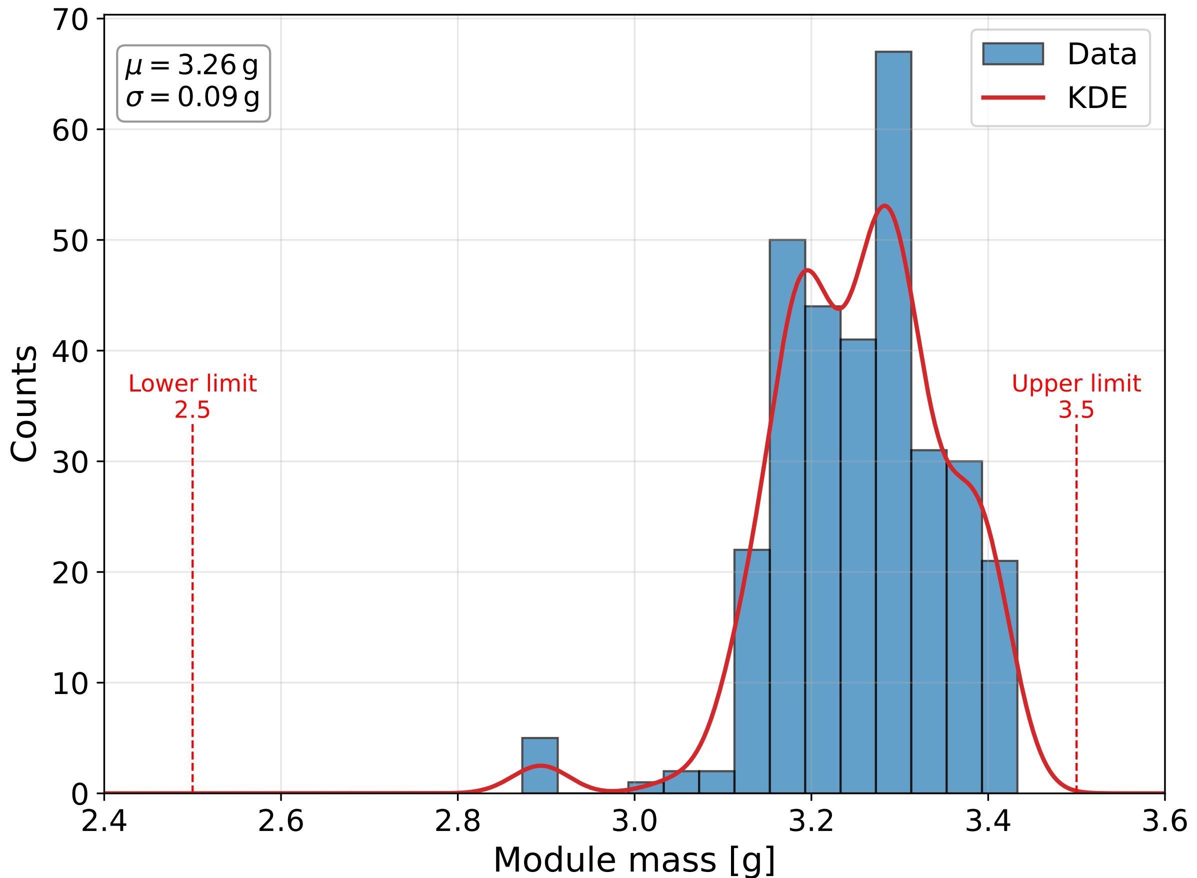


Figure 7.4.: Module mass distribution with KDE and limits.

## 7.5. Wire Bonding & Pull Testing

The chips and the flexes are interconnected via thin wire bonds. The nearly 190 wire bonds per chip are bonded in a programmed pattern. Certain parameters in the bonding process can adapt the loop shape of the wire bonds. There is a strict cut-off on the maximal loop height of the wire bonds at 750 $\mu$m. This strict specification ensures that there is no contact of the wire bonds with the OBWBP. So far, no module exceeded the maximal wire loop height during production. The mean loop height is measured to be $(632 \pm 54)\,\mu$m. Assuming a simple Gaussian model, it is expected that 1.4% of the production modules will be out of this specification. Note that there is a large uncertainty in the loop height measurement, since it is determined visually with the focus plane of the microscope

Some of the wire bonds are dedicated to being pulled to monitor the wire bonding quality by measuring the force required to pull off the wire bonds from the bonding pads. There

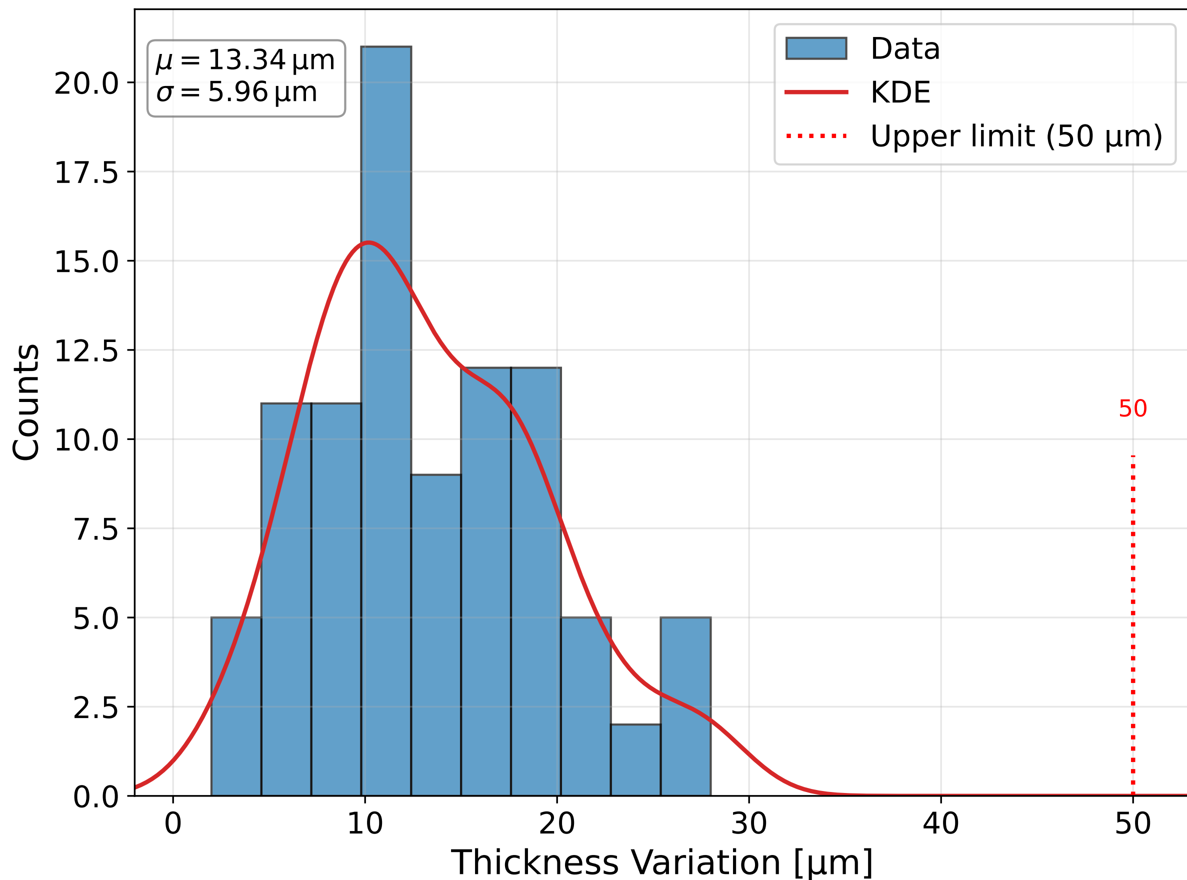


Figure 7.5.: Thickness variation between two measurement points on a Pixel module with KDE and limit.

are three quantities for each module that are determined: the maximal pull force value for a wirebond, the mean pull value over all the multiple wire bonds that are pulled on each module and the minimal pull value per module.

The mean value of the maximal pull testing is $(12.1 \pm 0.7)$ g with an extreme value of 13.35 g. The mean value of the average pull strength is $(10.8 \pm 0.8)$ g, as shown in Figure 7.7. The minimal pull force is on average $(8.4 \pm 2.1)$ g, as shown in Figure 7.8. There is a cut-off for the minimal required pull testing strength of at least 4 g. So far, only 3 modules have not met this requirement. Assuming the simplified model with $(\mu = (8.4 \pm 2.1)\,\text{g})$ it is expected that 1.9% of the production modules will not meet the minimal pull force. Since the upload of the pull values was changed during production, there is a limited statistic for the pull testing.

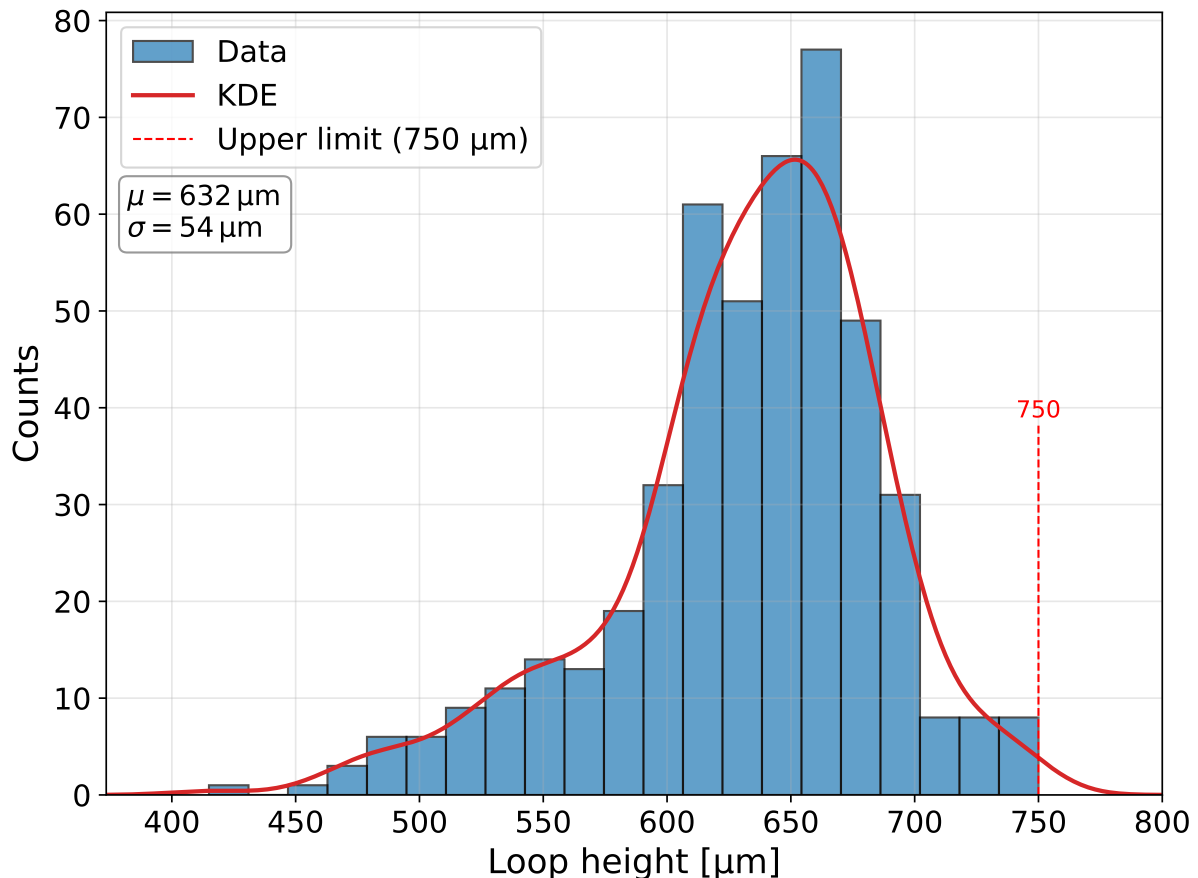


Figure 7.6.: Loop height distribution of the wire bonds with KDE and limit.

Figure 7.9 summarises all the production criteria with a specific cut-off. The specific values of the upper and lower limit are normalised to 1 and 0.

## 7.6. Masking & Parylene Coating

The modules are sent for Parylene coating either to APS in Paris or to the MPP in Munich. The module is covered with a Parylene layer, which mainly serves as an insulation layer between the sensor edge and the chips since the sensor is biased with high voltage. An additional advantage is the mechanical stabilisation of the fragile wire bonds. The Parylene coating is done by a sequential application of a first seed layer and then the actual Parylene layer. Both layers are applied in a strong vacuum required for the Parylene coating process in the machine, which is also the reason why the whole process takes several hours. The Parylene thickness and adhesion are monitored with a so-called test coupon, a silicon piece of similar module size, which is coated alongside the modules.
Since it is crucial to avoid Parylene coating at certain sensitive parts of the module, these

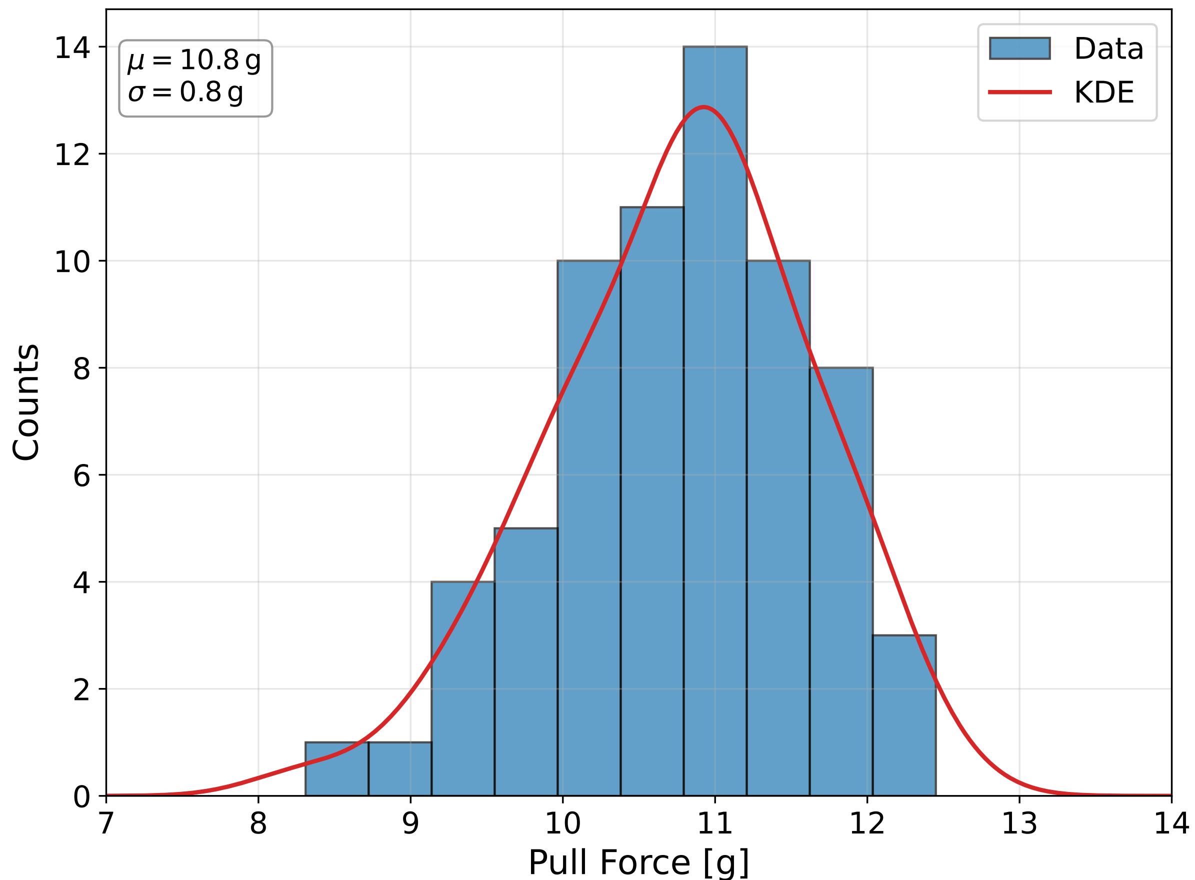


Figure 7.7.: Pull mean force distribution with KDE.

areas are masked. This includes the data and power adapter, which needs a reliable electrical connection for data and power transmission. On top of that, the pick-up points GA1-GA4 and the region of the strain reliefs are masked to glue the carbon canopies and the strain reliefs onto these points without gluing them on top of the flaky Parylene. The masking procedure is done on the second workbench. A vacuum tool is used to hold masking tape in place. Within the scope of this thesis, the masking tape design was improved. The cutting program *Silhouette Studio* is used to design the cut pattern of the blue-tape. As shown in Figure 7.10, before there were 4 pieces for front side masking, masking the pick up points and the connectors. Stannol and cap(s) are used for connectors. For the new design, the upper 3 blue tapes are merged. This novel design was first verified using a silicon dummy. The new design has the advantage of minimising the number of manual interaction steps in the masking and later the demasking. A novel, FTD in-house designed vacuum chuck was initialised within the scope of this thesis which is used to get air out of masking tape, especially on the backside.

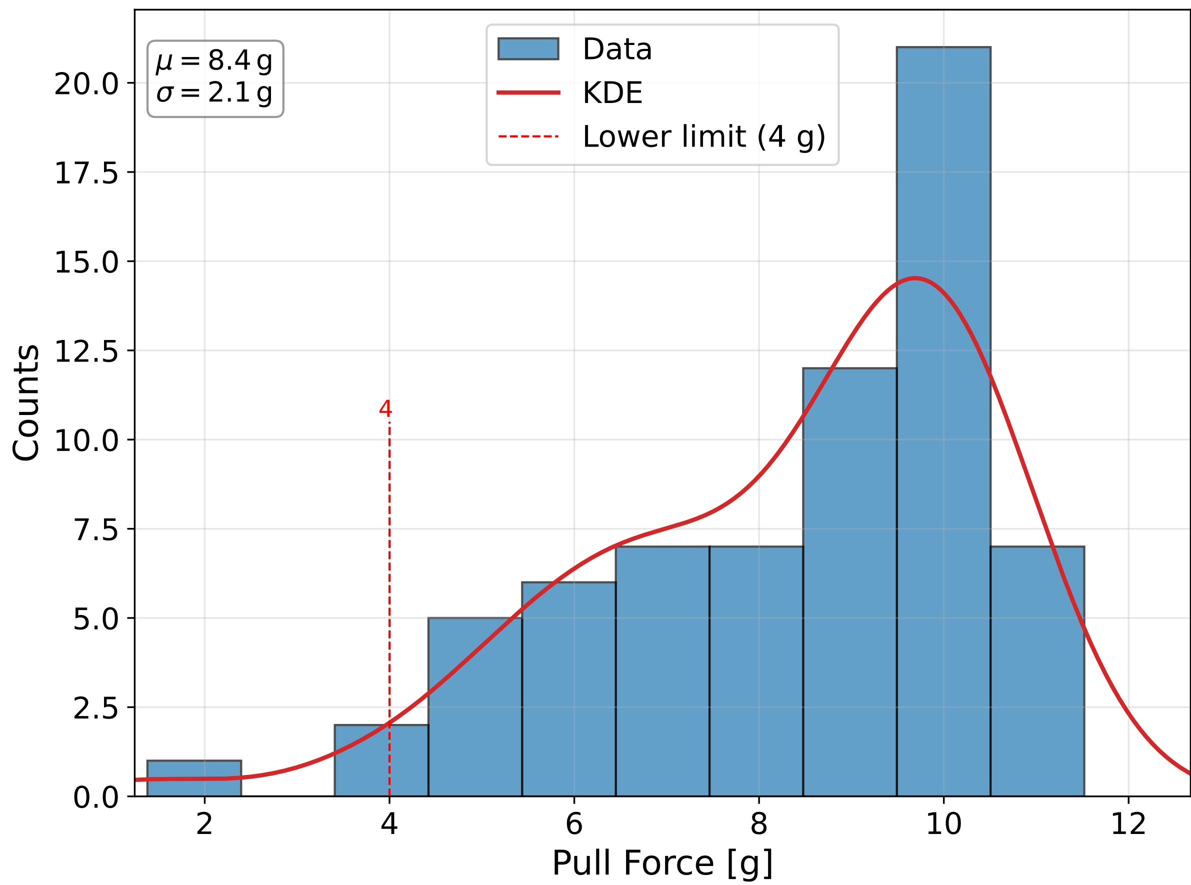


Figure 7.8.: Minimum pull values during pull testing with KDE and lower limit.

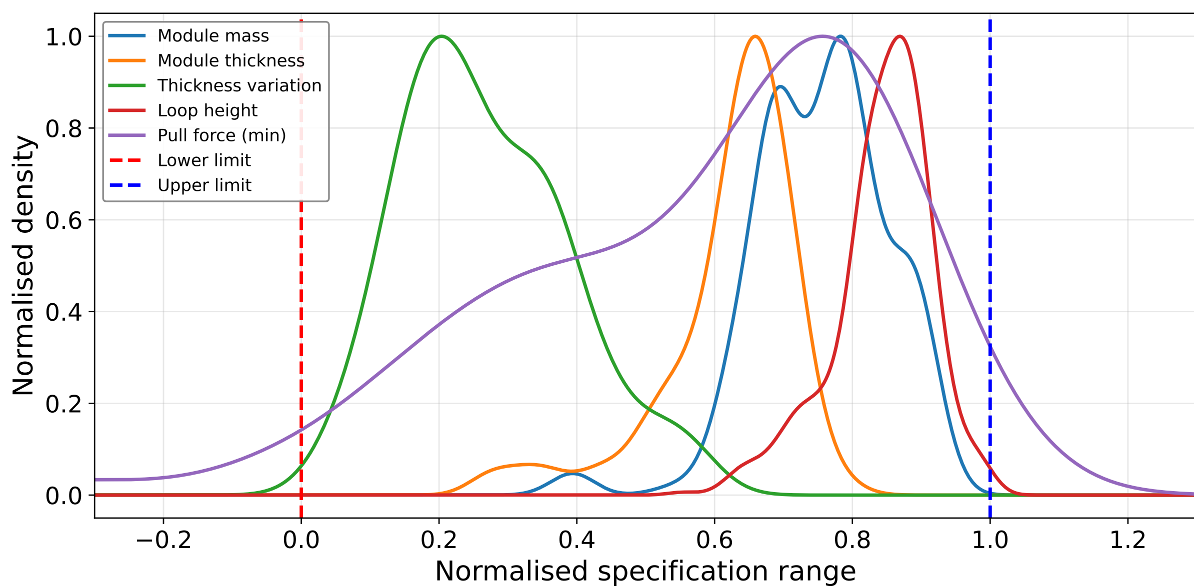


Figure 7.9.: Summary of all distribution which have an upper or lower limit.

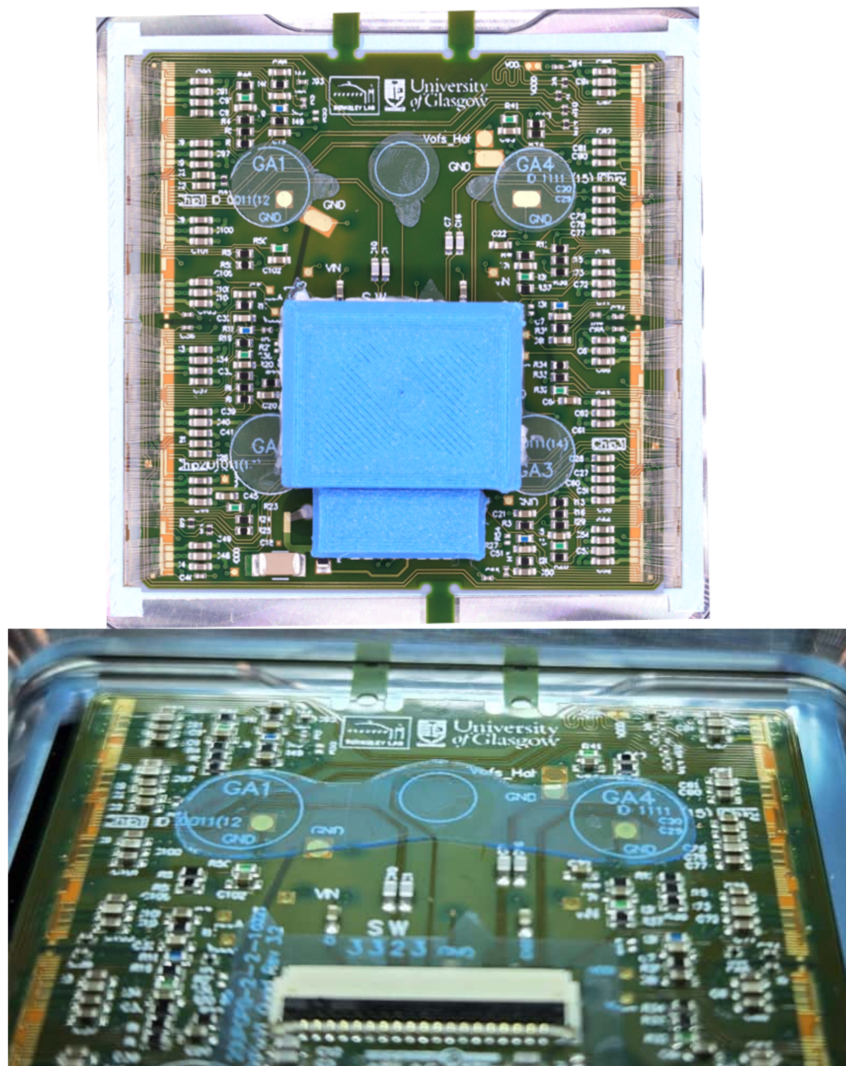


Figure 7.10.: Old and new design of the masking tape.

# 8. Electrical Quality Control

To secure reliable operation and high production standards particularly concerning the electrical properties and functionalities of the ITk Pixel modules, they are tested beforehand. Within the scope of the electrical module testing, there is the Cold Start-Up Test.

## 8.1. Cold Start-Up Test

The Cold Start-Up Test is a recently added electrical module test which addresses a previously untested operational scenario. It was identified that the ability of the modules to reliably start up at very low temperatures must be included in the electrical quality control (QC).
In the detector environment, the $CO_2$ cooling system initially cools the modules down to $-45\,°C$. The modules only reach their nominal operating temperature of $-15\,°C$ once the low voltage (LV) is powered on, due to self-heating.
This behaviour is not covered by the existing Final Cold test in module testing. In that test, modules are cooled from ambient conditions and maintained at a constant temperature of $-15\,°C$. A start-up from lower temperatures, such as $-45\,°C$, is therefore not probed. The constant temperature during the Final Cold test is maintained by a Peltier-based PID regulation system with controlled ambient conditions.
To close this gap in the electrical QC, the Cold Start-Up Test was developed. This test monitors the module temperature using the NTC sensor while cooling down to predefined target temperatures of $0\,°C$, $-10\,°C$, $-20\,°C$, $-35\,°C$, and $-45\,°C$.
Whenever a target temperature is reached within a tolerance of $\pm1$,°C, the following sequence is executed:

1. Record the module NTC temperature.
2. Power up the module by enabling the LV power supply.
3. Wait for 2 s to allow the system to stabilise.

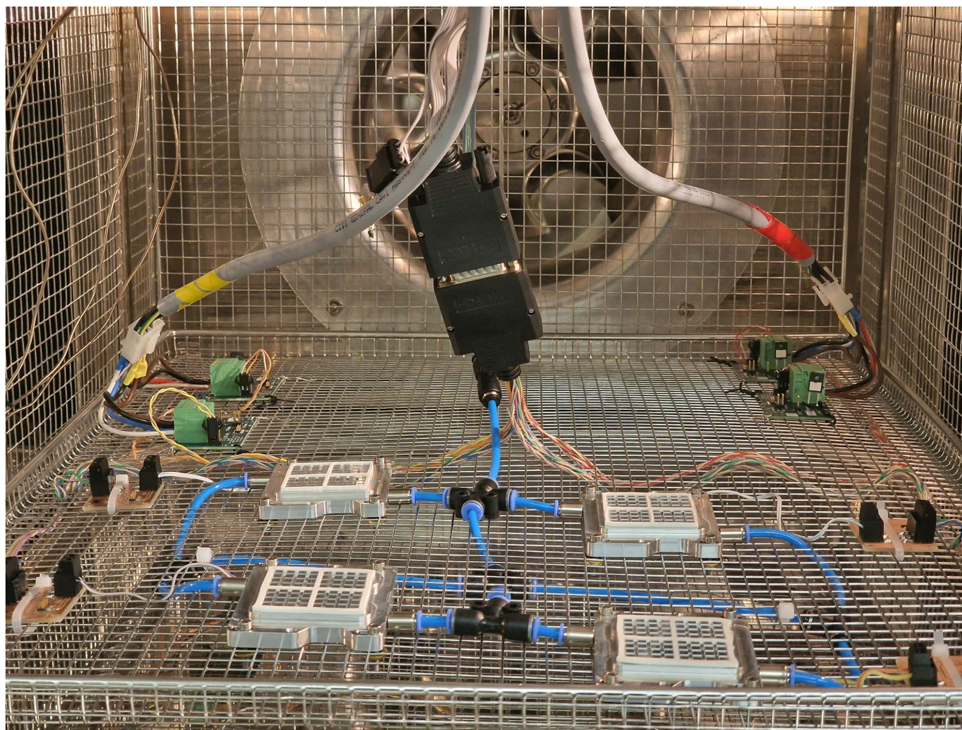

Figure 8.1.: Shock setup from the inside, used for thermal cycling and Cold Start-Up Tests.

4. Record the input voltage $V_{\text{in}}$ from the power supply.
5. Record the input current $I_{\text{in}}$ from the power supply.
6. Power down the module.

The recorded data are stored in a JSON file compatible with the format used for the SLDO scan output.

A module passes this test, if the difference in input voltage between warm and cold is less than 0.2 V.

## 8.2. Setup

The Cold Start-up Test is performed in a thermal shock chamber (*Vötsch VT 7012 S2*), which is additionally used for thermal cycling during production. Figure 8.1 shows the shock chamber setup.
A key requirement for this test is a stable LV power supply operating at 6.25 A in constant current mode. The chosen LV power supply is the *Keysight E3634A*, which provides a

25 V/7 A range. Studies by collaborators in the United States have shown that the ramp-up rate of the power supply significantly affects communication stability with the Pixel modules. It is therefore recommended to operate the LV power supply with a ramp rate exceeding $0.4\,\frac{\mathrm{V}}{\mathrm{ms}}$, which the *Keysight E3634A* can stably provide. The power supply is remotely controlled via GPIB. To enable the Cold Start-up Test in this setup, it is necessary to additionally monitor the input voltage $V_{\mathrm{in}}$.
A testing limitation is that the Cold Start-up Test can only be executed on one module at a time, while multiple modules are cooled simultaneously to the same temperature in the shock chamber. As a workaround, the test sequence can be paused at each temperature step and later resumed by iterating over up to 4 modules within the chamber.
The implementation developed during the internship by Thibaut Carouge provides 4 dedicated Cold Start-up Test slots, which feature relay-controlled sequential testing, in addition to the 4 thermal cycling slots of the chamber. Sense wires are used to compensate for voltage drops along the supply cables. The InfluxDB system is used to monitor temperature cycles between −45 °C and +20 °C for comparison.

## 8.3. Measurements and Results

So far, no module in production has failed the Cold Start-Up Test. As shown in Figure 8.2. The plot also shows that no correlation between the temperature difference and the input voltage difference can be observed.
Next, Figure 8.3 shows the distribution of the $V_{\mathrm{in}}$ differences. The mean voltage difference between warm and cold is $(58 \pm 14)$ mV. The upper limit of 200 mV is far beyond the hitherto measured voltage differences.

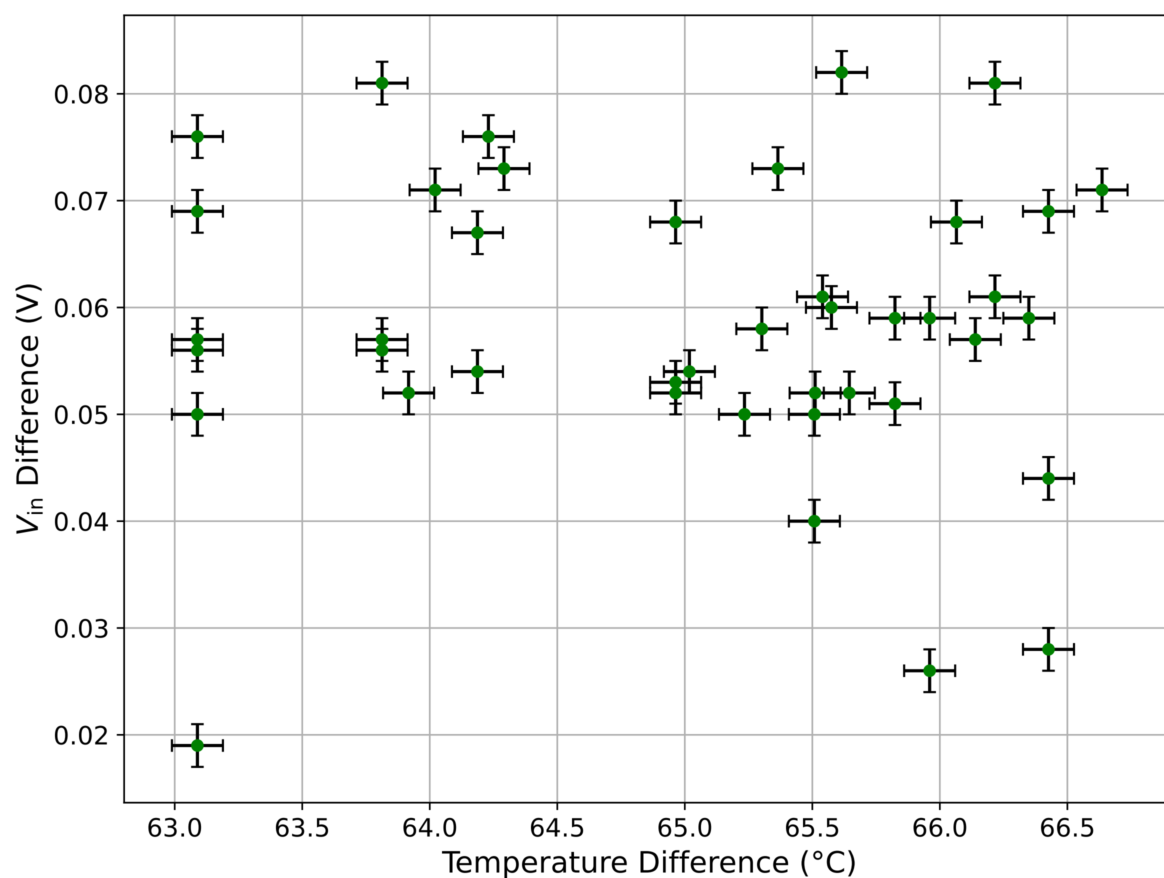


Figure 8.2.: Difference between warm and cold input voltage plotted against the temperature difference between the two voltage measurements. No correlation between the difference in $V_{in}$ and the temperature difference can be observed. The uncertainty of the temperature difference is assumed to be 0.1 °C, the uncertainty of the voltage difference is assumed to be 0.002 V.

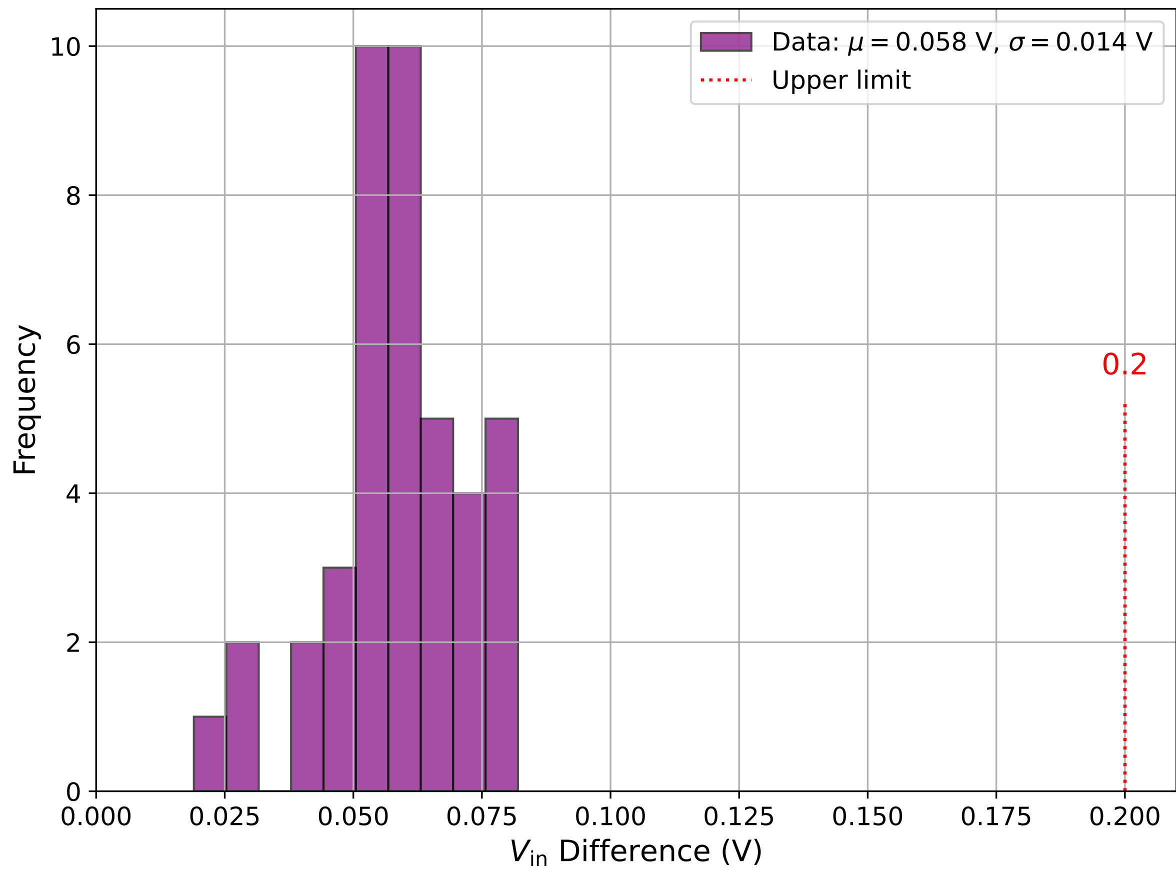


Figure 8.3.: Distribution of the $V_{in}$ differences measured during the Cold Start-Up Test.

# 9. Conclusion and Outlook

The HL-LHC will open a new chapter in hadron collider physics. The ATLAS experiment can only fully profit from the enormous efforts put into the accelerator upgrade if the ITk system, which in the past showed further delays, can make it in time and with a high production yield. The harsh radiation environment close to the beam pipe demands the new Pixel Detectors in ITk to operate in extreme conditions.

Module production in the German Cluster successfully started, and the work conducted during this thesis was part of it. The analysis showed, that the results of the gluing tools agree with each other and are well within the specs. The bonding also mostly meets the requirements but is limited in available statistics. Several improvements to the production infrastructure have already positively impacted the workflow. In particular, the optimisation of the probe station has significantly improved the production flow and facilitated BM reception, which remains crucial given the recurring issue of sensor cracking. The introduction of a new blue tape design, validated using dummy modules, has been established as the standard masking procedure in production. After successful qualification, this improvement has also been shared with other institutes, thereby contributing positively to the global ITk module production effort.

Also, newcomers are now trained with the detailed production guide, written within the scope of this thesis, which can be found in the Appendix A.

A key challenge for the ongoing ITk Pixel module production is the need to increase throughput in order to meet the strict project timelines. Several factors contribute to current production constraints. Delays in BM delivery have occurred, partly due to technical issues such as a broken laser at IZM. In the Outer Barrel production, a major bottleneck is the limited availability of carbon canopy tooling, with Siegen taking responsibility for the production of additional tools. Furthermore, the Parylene coating process introduces significant waiting times and enforces a batch-wise production scheme, limiting continuous throughput.

Within this context, production yield is becoming a key parameter for overall efficiency. A sufficiently high yield would allow a reduction in intermediate testing steps, thereby accelerating the production flow without compromising quality. In fact, several measurement

steps and specification cuts have already been phased out, and the results of this thesis suggest that further reduction of testing may be possible. This includes, for example, the observation that module thickness is consistently well within specifications and that the module mass measurement appears to provide limited additional value for production quality assurance.
Other monitoring quantities, such as loop height measurements, remain useful for assessing bonding quality. Although these values are affected by optical measurement uncertainties, they still provide a meaningful indication, especially since values close to the cut-off criteria are observed frequently.

In the context of Serial Powering, the $k$-factor measurements contributed to a deeper understanding of the chips' shunt current distribution and behaviour. The temperature stability within a few per cent could be confirmed, which is a good sign given the large temperature range during production. Also, the determination of the $k$-factors in the way that the residual current is minimised and the offset current is corrected seems promising for future measurements. The measurements in general are lacking statistics, since only a few single chip card setups have been dedicated to this kind of test.
In a next step, the mirror current measurements should be done with a quad module. It is more difficult to extract the $k$-factors, since the mux can not directly be accessed via a single chip card. This challenge was taken over by chip experts in Berkeley.

So far, no module has failed the cold startup test. These promising results will need to be confirmed with more extensive statistics. Also, the Cold Startup test done, as of today in Göttingen, only measures the voltage at -45°C and +20°C and not yet at the targeted temperatures of 0,-10,-20 and -35 °C which provides further information especially in case a module fails this test. Moreover, the current shock chamber setup is extended. The additional 4 chucks in the shock chamber are currently undergoing an upgrade within the scope of an internship, such that they also finally can perform the cold startup test. This will maximise the Göttingen module testing capacity such that the site is fully prepared for an increase in production module throughput.

# Bibliography

[1] S. L. Glashow, *Partial Symmetries of Weak Interactions*, Nucl. Phys. **22**, 579 (1961)

[2] S. Weinberg, *A Model of Leptons*, Phys. Rev. Lett. **19**, 1264 (1967)

[3] A. Salam, *Weak and Electromagnetic Interactions*, Almqvist & Wiksell, Stockholm, nobel symposium 8 edition (1968)

[4] S. L. Glashow, J. Iliopoulos, L. Maiani, *Weak Interactions with Lepton-Hadron Symmetry*, Phys. Rev. D **2**, 1285 (1970)

[5] H. Georgi, S. L. Glashow, *Unified Weak and Electromagnetic Interactions without Neutral Currents*, Phys. Rev. Lett. **28**, 1494 (1972)

[6] H. D. Politzer, *Reliable Perturbative Results for Strong Interactions*, Phys. Rev. Lett. **30**, 1346 (1973)

[7] H. D. Politzer, *Asymptotic Freedom: An Approach to Strong Interactions*, Phys. Rept. **14**, 129 (1974)

[8] D. J. Gross, F. Wilczek, *Asymptotically Free Gauge Theories*, Phys. Rev. D **8**, 3633 (1973)

[9] S. Weinberg, *The Making of the Standard Model*, Eur. Phys. J. C **34**, 5 (2004)

[10] G. 't Hooft, *Renormalization of massless Yang-Mills fields*, Nucl. Phys. B **33(1)**, 173 (1971)

[11] G. 't Hooft, *Renormalizable Lagrangians For Massive Yang-Mills Fields*, Nucl. Phys. B **35**, 167 (1971)

[12] G. 't Hooft, M. Veltmann, *Regularization And Renormalization Of Gauge Fields*, Nucl. Phys. B **44**, 189 (1972)

[13] G. 't Hooft, M. Veltmann, *Combinatorics of gauge fields*, Nucl. Phys. B **50**, 318 (1972)

[14] E. Noether, *Invariante Variationsprobleme*, Gött. Nachr. Math. Phys. Klass. (1918)

[15] H. Fritzsch, M. Gell-Mann, H. Leutwyler, *Advantages of the color octet gluon picture*, Phys. Lett. B **47(4)**, 365 (1973)

[16] M. Gell-Mann, *A Schematic Model of Baryons and Mesons*, Phys. Lett. **8**, 214 (1964)

[17] S. Tomonaga, *On a Relativistically Invariant Formulation of the Quantum Theory of Wave Fields*, Prog. Theor. Phys. **1(2)**, 27 (1946)

[18] J. Schwinger, *On Quantum-Electrodynamics and the Magnetic Moment of the Electron*, Phys. Rev. **73**, 416 (1948)

[19] J. Schwinger, *Quantum Electrodynamics. I. A Covariant Formulation*, Phys. Rev. **74**, 1439 (1948)

[20] R. P. Feynman, *Space-Time Approach to Quantum Electrodynamics*, Phys. Rev. **76**, 769 (1949)

[21] R. P. Feynman, *The Theory of Positrons*, Phys. Rev. **76**, 749 (1949)

[22] R. P. Feynman, *Mathematical Formulation of the Quantum Theory of Electromagnetic Interaction*, Phys. Rev. **80**, 440 (1950)

[23] F. J. Dyson, *The Radiation Theories of Tomonaga, Schwinger, and Feynman*, Phys. Rev. **75**, 486 (1949)

[24] F. J. Dyson, *The S Matrix in Quantum Electrodynamics*, Phys. Rev. **75**, 1736 (1949)

[25] ATLAS Collaboration, *Observation of a new particle in the search for the Standard Model Higgs boson with the ATLAS detector at the LHC*, Phys. Lett. B **716**, 1 (2012)

[26] CMS Collaboration, *Observation of a New Boson at a Mass of 125 GeV with the CMS Experiment at the LHC*, Phys. Lett. B **716**, 30 (2012)

[27] P. W. Higgs, *Broken Symmetries, Massless Particles and Gauge Fields*, Phys. Lett. **12**, 132 (1964)

[28] F. Englert, R. Brout, *Broken Symmetry and the Mass of Gauge Vector Mesons*, Phys. Rev. Lett. **13**, 321 (1964)

[29] G. S. Guralnik, C. R. Hagen, T. W. B. Kibble, *Global Conservation Laws and Massless Particles*, Phys. Rev. Lett. **13**, 585 (1964)

[30] G. S. Guralnik, C. R. Hagen, T. W. B. Kibble, *Global Conservation Laws and Massless Particles*, Phys. Rev. Lett. **13**, 585 (1964)

[31] P. W. Higgs, *Spontaneous Symmetry Breakdown without Massless Bosons*, Phys. Rev. **145**, 1156 (1966)

[32] T. W. B. Kibble, *Symmetry Breaking in Non-Abelian Gauge Theories*, Phys. Rev. **155**, 1554 (1967)

[33] S. H. Aulich, *Accessing Quantum Entanglement in off-shell $H \to ZZ$ with Separation of Polarisation States*, Bachelor thesis, II.Physik-UniGö-BSc-2023/05 (2023)

[34] R. L. Workman, et al. (Particle Data Group), *Review of Particle Physics*, PTEP **2022**, 083C01 (2022)

[35] O. Aberle, et al., *High-Luminosity Large Hadron Collider (HL-LHC): Technical design report*, Technical Report CERN-2020-010, Geneva (2020)

[36] ATLAS Collaboration, *Public ATLAS Online Luminosity Plots for Run-3 of the LHC*, `https://twiki.cern.ch/twiki/bin/view/AtlasPublic/LuminosityPublicResultsRun3` (2025), accessed: 2026-03-25

[37] O. Brüning, L. Rossi, *The High Luminosity Large Hadron Collider*, World Scientific (2024)

[38] ATLAS Collaboration, *ATLAS magnet system: Technical Design Report. Vol. 1. Technical Design Report*, Technical report, CERN, Geneva (1997), URL `https://cds.cern.ch/record/338080`

[39] ATLAS Collaboration, *The ATLAS Experiment at the CERN Large Hadron Collider*, JINST **3**, S08003 (2008)

[40] H. A. Lorentz, *La théorie électromagnétique de Maxwell et son application aux corps mouvants*, Archives Néerlandaises des Sciences Exactes et Naturelles **25** (1892)

[41] ATLAS collaboration, *The ATLAS Experiment at the CERN Large Hadron Collider*, JINST **3**, S08003 (2008)

[42] ATLAS Collaboration, *ATLAS Pixel Detector Electronics and Sensors*, JINST **3**, P07007 (2008)

[43] A. Ahmad, et al., *The silicon microstrip sensors of the ATLAS semiconductor tracker*, Nucl. Instrum. Meth. A **578**, 98 (2007)

[44] B. Mindur (ATLAS), *ATLAS Transition Radiation Tracker (TRT): Straw tubes for tracking and particle identification at the Large Hadron Collider*, Nucl. Instrum. Meth. A **845**, 257 (2017)

[45] N. Belyaev, et al., *Development of Transition Radiation Detectors for hadron identification at TeV energy scale*, J. Phys. Conf. Ser. **1390(1)**, 012126 (2019)

[46] H. Kolanoski, N. Wermes, *Particle Detectors*, Oxford University Press (2020)

[47] ATLAS Collaboration, *ATLAS Muon Spectrometer*, Technical Design Report CERN-LHCC-97-022, CERN, Geneva (1997)

[48] ATLAS Collaboration, *The ATLAS trigger system for LHC Run 3 and trigger performance in 2022*, JINST **19(06)**, P06029 (2024)

[49] M. Tanabashi et al. (Particle Data Group), *Review of Particle Physics*, Phys. Rev. D **98**, 030001 (2018)

[50] H. Bethe, *Zur Theorie des Durchgangs schneller Korpuskularstrahlen durch Materie*, An. Phys. **397(3)**, 325 (1930)

[51] F. Bloch, *Zur Bremsung rasch bewegter Teilchen beim Durchgang durch Materie*, Ann. Phys. **408(3)**, 285 (1933)

[52] M. Buzzo, M. Ciappa, W. Fichtner, *2D junction delineation for the failure analysis of silicon carbide devices* (2005)

[53] R. Nelms, R. Johnson, *200°C operation of a 500-W DC-DC converter utilizing power MOSFETs*, Industry Applications, IEEE Transactions on **33**, 1267 (1997)

[54] E. Young, *Ultrafast acoustic strain generation and effects in semiconductor nanostructures*, Ph.D. thesis (2014)

[55] W. Shockley, *Currents to Conductors Induced by a Moving Point Charge*, J. Appl. Phys. **9(10)**, 635 (2004)

[56] S. Ramo, *Currents Induced by Electron Motion*, Proceedings of the IRE **27(9)**, 584 (1939)

[57] D. A. Giugni, *Pixel Quad Module Assembly DWG*, Engineering Drawing, CERN Internal (2025), AT2-IP-ED-0010, v. 11, EDMS

[58] R. L. Bates, *Technical Specification for ITk Pixel Modules*, Specification Document, CERN Internal (2022), AT2-IP-ES-0009, v. 3, EDMS

[59] RD53 Collaboration, *RD53C Chip Manual*, Technical Report CERN-RD53-PUB-24-001, CERN, Geneva (2024)

[60] J. Kampkötter, et al., *Characterization and verification of the Shunt-LDO regulator and its protection circuits for serial powering of the ATLAS and CMS pixel detectors*, J. Phys. Conf. Ser. **2374(1)**, 012071 (2022)

[61] T. Heim, *YARR - A PCIe based readout concept for current and future ATLAS Pixel modules*, J. Phys. Conf. Ser. **898(3)**, 032053 (2017)

[62] R. Förster, *Quality Control Systems and Processes for ITk Module Production*, Master thesis, II.Physik-UniGö-MSc-2026/01 (2026)

[63] ATLAS Collaboration, *ATLAS ITk Production Database use and tools for the ITk Pixels community*, JINST **20(06)**, C06029 (2025)

[64] D. A. Feito, *Design Overview of the Loaded Local Supports for the ITk Pixel Outer Barrel*, Engineering Report, CERN Internal (2023), AT2-IP-ER-0046, v. 1, EDMS

[65] D. Freedman, P. Diaconis, *On the Histogram as a Density Estimator: L2 Theory*, Zeitschrift für Wahrscheinlichkeitstheorie und Verwandte Gebiete **57(4)**, 453 (1981)

[66] R. Bates, M. Wielers, I. P. C. Board, *Serial Number Specification for ITk Pixel Modules and its Components*, Technical Report AT2-IP-EP-0026, CERN (2025), rev. 3.3, EDMS 2649105

# A. Assembly Guide

## A.1. Flex Reception & Metrology

When the Flexes arrive at the institute, a first visual check is performed: are any SMD components missing or loose, are the last 4 digits of the Flex number in the top right corner similar to the 4 digits in the Flex centre between the power- and the data-adapter. If they are not the same, please contact Yannick.
In a first step, photos are taken from the Flex front- and backside. There is a dedicated photo station with metal chucks for both the front- and the backside of the Flex. It is best to clean the chucks with the pressured air before positioning the Flex on the chuck. Once the Flex is in position on the chuck, turn on the vacuum to keep it in place. Next, activate the camera, which will also automatically open a digital control panel on the connected Lab PC. Click on "Livebild aufnahme starten„, which will broadcast the live picture from the camera. Focus on the Flex on the chuck, using first of all the camera focus if needed, and use the wheel of the movable table underneath the chuck for fine adjustment.
Clean with dry air to clean any contamination.
Press the main button to take a picture of the flex. It is best to take all pictures from all Flex front sides first, and next all Flex back sides, such that the different chucks do not have to be switched all the time. There is a timer to minimise any vibrations on the setup.
The photos that were taken have to be renamed accordingly, and then they have to be sorted into the new Flex folders, which have to be created. "*Flex serial number*_front/back „Make sure the photo is well-oriented. The name of the folder is the Flex serial number. Next, copy the Flex Excel sheet from the "Vorlagen „folder into the Flex folder and also rename it according to the Flex serial number. Open this document and activate the editing mode.
The excel spread sheets provides an overview of the aspects that have to be measured as part of the Flex metrology. Enter the Flex serial number as well as the current date, the temperature and the humidity. Please carefully put the flex on the high-precision scale,

making sure that the scale shows 0 before the mass measurement. Note the Flex weight in the sheet. Next, measure the thickness of the 4 pick-up points (GA1-GA4) using the calliper gauge with the pointy cap. Aim for the golden ground pads for GA1 and GA4, and try to avoid the writings on GA2 and GA3. You will have to make sure the calliper gauge is reset to 0 when in the closed position. Note all 4 values in the sheet.
Next, determine the height of the capacitor and the power adapter base as shown in the pictures.
Next, prepare the chuck by cleaning it with pressurised dry air. Put the Flex on the chuck on the microscope. Secure contact with all three chuck pillars and turn on the vacuum. Turn on the microscope and the light. With the large screw on the side of the chuck, the Flex on the chuck can be aligned with the microscope cross-hair pointer.

Measure the x- and y-dimensions of the flex near both of the edges and in the Flex centre. In the end, store them in the Flex box in layers of 5, separated by clean room-compatible white sheets.

Overview:

- visual inspection, check serial number
- take photos front- and backside
- sort pictures in folder
- measure weight
- measure GA1-GA4 thickness with calliper gauge
- determine capacitor and power adapter height
- measure x- and y-dimensions with big microscope
- fill in excel sheet

## A.2. Bare Module Reception & Metrology

The Bare Modules (BMs) are Silicon sensors bump-bonded to radiation-hard readout chips. They arrive in gel packs.
Upon opening the gel packs, conduct a first check for major inconveniences such as bumps, scratches or cracks.
Take pictures of the modules in the gel packs. The entire gel pack can be positioned on the photo chuck. Adjust the camera focus if necessary. Take pictures from each BM, first of all, from the side that is facing up when they arrive. Next, the BM have to be rotated 90° clockwise and then they have to be flipped by 180°. Therefore, the gel pack has to be put on the vacuum chuck, and the vacuum needs to be activated. The BMs are picked up using the vacuum tweezers. For the flipping, put the BM in the Kapton envelope. Then, take photos from the BM front sides with the current orientation. Make sure not to rotate them any more, since the BM orientation is now right and important later in the process.
Next, the IV-curves of the BM are probed. Therefore, take the gel pack with the BM to the basement where the probe station is located.
There is the main switch at the bottom on the right side of the probe station. Open the lid by twisting the handle counterclockwise. The probe station has a movable chuck

and a movable microscope, both of which can be controlled via the joystick on the right. Sometimes this does not work, so simply use the control program on the connected PC. Clean the chuck before using it. lift up the probe needle via the screws at the top. The other two screws on the side control the x- and the y-axis position of the probe needle. The probe needles stick to the plate of the probe station via vacuum. If no other group has played around with the probe station, this position should not be modified. The needles usually face each other.
There is a vacuum chuck in the IV station, similar to the one in the clean room, to re-release the BMs. Next to it are vacuum tweezers to lift the BM from the gel pack to the chuck. Turn off the vacuum just millimetres above the chuck, to avoid a floating BM. Please do not change the orientation of the BM. Next, turn on the vacuum of the chuck, which will keep the BM in place.
There are different speeds for the camera and the chuck !
Align the microscope and camera with the left probe needle. If nobody changed the settings, one just has to move the chuck until one can see pad 11 in the camera. Then lower the probe needle until one can see the tip in the camera. The needle is not in proper contact until one can observe a lateral slide of it on the pad. In case the settings were not changed, the camera should now only be moved to the right until it is above the right needle. Now watch in the microscope or the camera and lower the right needle until it fully makes contact with the sensor (small slide on the sensor).
Now turn off the light and close the lid. In the program open on the PC, change the serial number of the BM accordingly and start the Python script in the terminal. Hopefully, the power supply is already activated. The IV scan runs automatically and takes about 15 min.
Once the scan is done open the lid again and turn on the light. now first of all lift the two probe needle (careful which direction to rotate the screws, one does not want to scratch the BM). In best case scenario, the home position of the microscope is aligned with the left probe needle such one only has to click the scope home position to watch the pad needle lift off.
Once the needles are lifted up, the chuck can be returned to its home position, which should be the central position closest to the probe station lid to best change the BM. Turn off the vacuum on the chuck and turn on the vacuum of the vacuum tweezer to proceed with the next BM until a gel pack is fully probed.
After taking all the IV curves, the folders with the BM serial number names are created. Sort the pictures taken from the BM into the appropriate folders. Additionally, copy the BM Excel sheet into the folders and rename them accordingly. fill out the BM serial

number, date, and humidity
Then put the BMs one by one into the Kapton envelope and measure the thickness in the area of the pick-up points. Use the digital calliper with the flat tip. Additionally, measure the weight of the BM with the high precision scale. next, place the BM onto the vacuum chuck under the microscope and secure it with vacuum. Measure the dimensions of the chip and the sensor according to the spreadsheet. When determining the chip dimensions, also check the hex code on the pads 7,60,112 and 165 on each chip. There is a dedicated spreadsheet to convert from binary to hex. The upper bit is always the one which is closest to the sensor. For the metrology, the cross-hair should be right on the corners of the chip or sensor. The blue buttons reset the scale to 0. Note all the dimensions in the spreadsheet and save it in the corresponding folder. Lastly, turn off the vacuum holding the BM in place and carefully put it back in the gel pack using the vacuum tweezers. Pay attention to not changing the orientation. Proceed with the next BM metrology. In the end, put the gel pack back into the dry air cabinet. report abnormalities asap. also maybe take a quick look at the IV curves to check if they look as expected.

Overview:

- visual inspection
- pictures from chip side
- rotated 90° clockwise and flip
- pictures from sensor side
- IV curves
- sort pictures in folders
- determine mass
- measure BM thickness in Kapton envelope with calliper
- put BM on big microscope, turn on vacuum
- measure Chip and Sensor dimensions
- determine hex codes per chip (pad 7, 60, 112 and 165)
- fill in spreadsheet

IV curve:

- switch on the probe station, power supply, vacuum pump and the PC, turn on light in the probestation
- lift up probe needles
- go to chuck home position
- clean chuck
- place gel pack on vacuum
- carefully use vacuum pick up tool to place one BM on the chuck
- activate chuck vacuum
- move chuck until you see pad 11 in the camera
- lower left probe needle and bring it to contact with pad 11
- move the scope in the right direction only until it is above the right needle
- take a look in the microscope, lower the right needle and make contact with the sensor
- turn off light and close the probe station
- enter serial number in the script, save it and run the IV scan script
- once it is done, open the probe station, turn on the light
- bring needles to topmost position
- bring microscope back to home position (aligned with left needle)
- go to chuck home position
- deactivate chuck vacuum
- pick up BM with vacuum tweezer and place it back in gel pack
- proceed with next module

### A.2.1. Vacuum Chuck Alignment

For all the components (Flex, BM and glued Module), metrology with the microscope has to be done at some point in the procedure. To secure reproducible measurements, there is a dedicated vacuum chuck to be installed on the microscope chuck. The vacuum chuck itself is held in place with vacuum on the microscope chuck. The orientation of the vacuum chuck can be adjusted using the big metal screw. Please make sure that the vacuum hoses are running well between the microscope oculars.
The three pins on the vacuum chuck, which serve as an orientation for the alignment, should be in the back and on the left from a user perspective. The Module and Flexes should be put onto the vacuum chuck such that the pins are between the green frame. The BM must be rotated by 90° counter-clockwise and is just aligned when in contact with the pins. Once the BM, Flex or Module are in place on the vacuum chuck, turn on the vacuum to fix it. Now one has to align the BM, Flex or Module with the vacuum chuck on the microscope with the crosshair of the microscope. Go to one of the upper corners of the BM, Flex or Module and search for some straight structures, such as a trace or the BM or Flex or Module edge. Try to align the chosen structure with the microscope crosshair as closely as possible in the visible part. Use the big metal screw to rotate the vacuum chuck. Now, follow the structure under the microscope to the opposite side by turning the microscope chuck handle. The offset that you now see between the microscope crosshair and your chosen structure can be minimised step by step, by adjusting the vacuum chuck's orientation on the microscope to half the offset one observes now and then compensating with an adjustment of the microscope chuck afterwards. Repeat this step until the BM, Flex or Module on the vacuum chuck is well aligned with the microscope crosshair, and one can follow a chosen linear structure, such as the edge from left to right, without losing the crosshair alignment with it.

Overview:

- place vacuum chuck on a paper on the big microscope
- turn on bottom vacuum to hold it in place
- turn on microscope and light
- tune alignment via large metal wheel with large linear structures until crosshair of the microscope is parallel to the vacuum chuck

## A.3. Module Assembly

### A.3.1. Preparation

To prepare for the Module Assembly, firstly look up the Flex and the BM serial number that will be clued together and send them to Yannick such that he can generate the according module number. Roughly 2-3 hours before starting the glueing process, one should turn on the heating plates at 60°C to warm up the module gluing tool. Clean the tip of the vacuum tweezer in preparation of the assembly process. Also blow away potential particles on the BMs in the gel pack using the compressed dry air.

Once the assembly tools is well warmed up, carefully take off the single components and place them next to the hotplate on the assembly table. Next, Prepare the

- prepare BM and Flexes, a list and serial numbers
- carefully unmount preheated tool
- double check for HV cover on topside of flex
- place flex in flex jig, use block and turn on vacuum
- switch on gauge, lift up module jig to topmost position, large button clockwise
- turn fine adjust also to topmost position counter-clockwise
- place module on clean jig and turn on vacuum
- bring module jig to lowest position, large button counter-clockwise
- mate both jigs, fasten 2 screwa
- lift up module jig via large button to topmost position clockwise (contact flex and BM)
- reset gauge to zero
- turn fine adjust clockwise lowering the module (approx. 11 rotations before visible input) and set glue gap (370)
- separate both jigs
- mount stencil clamp

- mix glue 5:4 (2,5:2 g), apply between sloped spatula side
- apply glue via spatula, 20 seconds
- carefully dismount glue stencil
- mount flex jig bakc on module jig and fasten screws
- cure glue for at least 8 hours
- measure weight, GA1-GA4 thickness and alignment
- fill in excel sheet

## A.4. Masking

First, place a large piece of blue tape on the vacuum chuck. Then load four small pieces of blue tape onto the second vacuum chuck. Remove the bottom of the carrier and press the module backside onto the blue tape. Afterward, deactivate the vacuum. Place a small piece of paper into the carrier and mount the chuck backside. Remove the carrier lid and press it onto the blue tape, then deactivate the vacuum again. Store the module under vacuum for at least 30 minutes. After this, press out any air bubbles trapped underneath the stickers and store the module under vacuum once more. Open the lid and apply wirebond protection. Add Stannol to the rim of the blue cap, then attach the cap to the data adapter. Apply Stannol also to the power adapter. Switch the carrier lids to the two pillar lids and turn off the pressurized air. Finally, take pictures of the setup and place the module in the carrier, then vacuum-pack everything in red foil.

Overview:

- big blue tape on vacuum chuck
- load 4 small blue tape pieces on second vacuum chuck
- remove carrier bottom
- press module backside on blue tape and deactivate vacuum
- little paper in carrier and mount chuck backside
- remove carrier lid and press on blue tape

- deactivate vacuum
- store module under vacuum, at least 30 min
- press out air bubbles from underneath the stickers
- store under vacuum again
- open lid and put on wirebond protection
- Stannol in blue cap rim
- put cap on data adapter
- put Stannol on power adapter
- switch carrier lids to two pillar lids
- turn off pressured air
- take pictures and put module in carrier in vacuum-pack in red foil

## A.5. OBWBP

Start by weighing the canopies and recording their respective numbers. Then measure GA1–GA4 (pillars) and, if necessary, determine the resistivity. Ensure that the module has been fully measured and that all required previous photos have been taken. Install the pins according to the reference picture, ensuring the correct diameters are used. Remove the pig tails from the module and dismount the module from the carrier. Center the module on the tool and activate the vacuum. In parallel, center the canopies on the tool and also activate the vacuum. Prepare the adhesive mixture with a 10:8 ratio (2.5 g : 2 g), ideally synchronizing this step with the module assembly. In parallel, prepare the silver conductive adhesive. Mount the stencil and apply the glue. Afterwards, remove both the stencil and the frame. Place the tool jigs onto the hotplate and cure for several hours, depending on the hotplate temperature. After curing, measure the GA1–GA4 thickness again and take a front-side photo of the module. Finally, fill in the corresponding Excel sheet.

Overview

- weight canopies and note the respective number

- measure GA1-GA4 (pillars), eventually measure resistivity
- make sure the module is measured and all previous photos are taken
- install pins according to picture with according diameter
- remove pig tails from module and dismount module from carrier
- centre module on the tool and turn on vacuum
- centre canopies on tool and turn on vacuum
- mix glue 10:8 (2,5:2 g) ideally time with module assembly
- mix silver conductive adhesive
- mount stencil and apply glue
- unmount stencil and frame
- mate tool jigs on hotplate for several hours depending on hotplate temperature
- measure GA1-GA4 thickness and take front side photo
- fill in excel sheet

# Acknowledgements

First of all, I would like to express my sincere gratitude to Prof. Dr. Arnulf Quadt for giving me the opportunity to work on such an interesting topic and for his continuous support throughout the years. He did not just supervise my Bachelors and Masters, but also opened many doors for me.
Next, I would also like to thank Prof. Dr. Jörn Große-Knetter for beeing once again my second referee and for always taking the time to answer my questions and for ensuring the smooth operation of the lab.
Many thanks go to Ruben Förster for his tireless work in the lab and for the many entertaining conversations.
I am very grateful to the entire ITk team, especially the students, whose collective efforts make the production in Göttingen possible.
I would like to thank the LBNL ATLAS team in Berkeley for warmly welcoming me to their institute and making my master's experience truly special. In particular, I would like to thank Timon Heim, Deion Fellers, and Elisabetta Pianori.
I also wish to thank Prof. Dr. Jochen Dingfelder and the entire Bonn SiLab team for hosting me in their group and for providing excellent facilities at the FTD in Bonn. In particular, I would like to thank Yannick Dieter, as well as the dream team Walter and Wolfgang.
Furthermore, I would like to thank the group of Prof. Quadt at the II. Institute of Physics for the collaborative and inspiring work over the past years.
I am also grateful to the Glaskasten friend group for making my university studies much more enjoyable, especially my dear Simi.
Finally, I would like to thank my wonderful fiancée Anni for her endless support, encouragement, and love. Meeting you has made my life better in every possible way.

# Erklärung zur Nutzung von ChatGPT und vergleichbaren Werkzeugen im Rahmen von Prüfungen

In der hier vorliegenden Arbeit habe ich ChatGPT oder eine andere KI wie folgt genutzt:

- ❑ gar nicht
- ❑ bei der Ideenfindung
- ❑ bei der Erstellung der Gliederung
- ❑ zum Erstellen einzelner Passagen, insgesamt im Umfang von ______________% am gesamten Text
- ❑ zur Entwicklung von Software-Quelltexten
- ❑ zur Optimierung oder Umstrukturierung von Software-Quelltexten
- ❑ zum Korrekturlesen oder Optimieren
- ❑ Weiteres, nämlich: ______________________________________

Ich versichere, alle Nutzungen vollständig angegeben zu haben. Fehlende oder fehlerhafte Angaben werden als Täuschungsversuch gewertet.

____________________________________

Niklas Grün
28th of April 2026

**Erklärung** nach §17(9) der Prüfungsordnung für den Bachelor-Studiengang Physik und den Master-Studiengang Physik an der Universität Göttingen:

Hiermit erkläre ich, dass ich diese Abschlussarbeit selbständig verfasst habe, keine anderen als die angegebenen Quellen und Hilfsmittel benutzt habe und alle Stellen, die wörtlich oder sinngemäß aus veröffentlichten Schriften entnommen wurden, als solche kenntlich gemacht habe.

Darüberhinaus erkläre ich, dass diese Abschlussarbeit nicht, auch nicht auszugsweise, im Rahmen einer nichtbestandenen Prüfung an dieser oder einer anderen Hochschule eingereicht wurde.

Göttingen, den 28. April 2026

(Niklas Grün)